



NTNU Trondheim
Norwegian University of Science and Technology
Department of Marine Technology

MASTER THESIS IN MARINE CYBERNETICS

SPRING 2017

FOR

STUD. TECH. Aksel Stadler Kjetså

Localisation of Submarine Power Cables by Magnetometers on REMUS 100 AUV

Motivation and work description

Statnett SF is the system operator in the Norwegian energy system. They install and maintain several underwater power lines throughout Norway. The cables are prone to damage from the environment and human activities. Sections that are close to, or above, the seabed are especially vulnerable. A part of maintaining the cables is to carry out underwater surveys. These surveys should ensure that the cables are properly buried, and inspect for signs of damage. Today, Statnett SF uses Remote Operated Vehicles (ROVs) combined with cameras to survey the cables. This is both tedious and expensive. Potentially, using an autonomous underwater vehicle (AUV) to locate, and track, the cables by their magnetic field could significantly reduce the time and costs.

The aim of this thesis is to review, design and implement methods for submarine cable localisation by magnetic sensors. In addition, routines for correct calibration of the magnetometers should be established and implemented.

Another thesis, which regards designing and implementing control systems for cable tracking on REMUS 100 AUV, was initiated in conjunction with this thesis. Ideally, they should together be able to carry out an AUV-based cable survey by magnetic-based guidance.

Scope of work

- Derive an expression for the magnetic field around a single AC cables
- Derive an expression for the magnetic field around AC cables in a three-phase power system
- Formulate methods for cable localisation of submarine cables by the magnetic field they produce.
- Establish routines for correct calibration the magnetometers
- Set up a finite element analysis of a relevant set of cables and test the methods on the simulated magnetic field
- Create a device that can be mounted on REMUS 100AUV to carry out a magnetic-based cable survey
- Implement the cable localisation methods on the created device and test the methods



NTNU Trondheim
Norwegian University of Science and Technology
Department of Marine Technology

- Implement and test the magnetometer calibration routines on REMUS 100 AUV

Supervisor: Professor Martin Ludvigsen

Co-supervisor: Phd-candidate Petter Norgren

Co-supervisor: Statnett SF engineer Anders Ballari

Abstract

Power cables that are exposed to the marine environment are prone to damage, especially if they are located close to, or above, the seabed. Underwater surveys are carried out to ensure that cables are buried and inspect for signs of damage. Today, Statnett SF perform surveys by ROVs and underwater cameras, this is both tedious and expensive. Using AUVs to locate and track the cables based on their magnetic field, could lead to cost reductions. Several commercial products exist for this purpose, however, most of them are developed for telecommunication cables and they are not always applicable for three-phase power systems.

In this thesis, a mathematical model is derived for the magnetic field around a three-phase power system, and verified by comparison to finite element analysis. Further, the model is used to design and implement a method to track and locate all cables in a three-phase power system. Both simulations and experiments confirms that the method is accurate when locating the cables. For cable tracking, the method is accurate when on either side of the three-phase power system. When in-between the cables, there is a risk of a wrong direction being given. Nevertheless, it is shown that this do not happen either for simulations or experiments.

Today's commercially available solutions for cable tracking, locates the cables in a three-phase power system by assuming the closest is an independent cable. This method give erroneous results when the cables are too close. By simulations it's concluded that erroneous results occurs when the distance between the cables is less than 8 times the AUVs hover height over the same cables. This is, however, dependent on cable specific parameters and the accuracy of the magnetometers.

A device for carrying out magnetic-based cable survey is developed and implemented on REMUS 100 AUV. This includes a method to locate single cables, cables in a three-phase power

system as well as a calibration routine for the magnetometers. All experiments are carried out with this device and the results from these concurs with that of the simulations. Lastly, it is shown that the calibration routine successfully calibrates for ferromagnetic distortions as well as for misaligned sensors.

Sammendrag

Undersjøiske strømkabler er sårbare mot skade fra det maritime miljøet, spesielt kabler som er helt eller delvis på overflaten av havbunnen. Undervannsundersøkelser gjennomføres for å sikre at kablene er godt nok begravd og for å inspisere etter skade. I dag utfører Statnett SF undersøkelser ved hjelp av ROV og undervannskameraer, dette er både tidkrevende og dyrt. Det kan spares ved å i stedet bruke en AUV som sporar kabelen basert på magnetfeltet dens. Flere kommersielle produkter eksisterer alt for dette formålet, men de fleste er utviklet for telekommunikasjonskabler, og er ikke alltid anvendbare for tre kabler i et trefaset strømsystem.

I denne oppgaven er en matematisk modell utledet for magnetfeltet rundt et trefaset strømsystem. Denne er så verifisert i sammenligning med en analyse basert på elementmetoden. Videre brukes denne modellen til å designe, og å implementere en metode for å spore og lokalisere alle kabler i et trefaset strømsystem. Både simuleringer og eksperimenter bekrefter at metoden er nøyaktig angående lokalisering av kablene. For kabelsporing er metoden nøyaktig når AUV'en er på en side av alle kablene. Når den er mellom kablene, er det fare for at feil retning blir gitt. Imidlertid skjedde ikke dette verken i simuleringer eller eksperimenter.

Dagens kommersielle produkter lokaliserer kablene i et trefaset kraftsystem ved å anta at den nærmeste som en uavhengig enfaset kabel. Denne metoden vil få betydelige feil hvis kablene er for nære hverandre. Ved simuleringer ble det konkludert at for nært er om avstanden mellom kablene er mindre enn 8 ganger AUVens høyde over de samme kablene. Dette er imidlertid avhengig av kabelspesifikke parametere og nøyaktigheten til magnetometrene.

Et apparat for utføre magnetisk basert kabelundersøkelse er utviklet og implementert på REMUS 100 AUV. Dette inkluderer en metode for å lokalisere enkeltkabler, kabler i et trefaset

strømsystem, samt en kalibreringsrutine for magnetometrene. Alle eksperimenter utføres med dette apparatet, og resultatene fra disse er i samsvar med simuleringene. Til slutt er det vist at kalibreringsrutinen med lykkes med å kompensere for ferromagnetiske forstyrrelser, samt for feiljusterte sensorer.

Preface

This master thesis was written during the spring of 2017 and is the last part of a Master of Science degree at the department of Marine Technology at the Norwegian University of Science and Technology. This thesis was written in collaboration with Statnett SF and was initiated by a preliminary project thesis, written during the fall of 2016. The main concern of this master thesis is the detection and localisation of submarine power cables by the use of magnetometers on REMUS 100 AUV. Statnett SF motivated to this thesis by a desire to perform cheaper, and faster, surveys on such cables. The main topic is to design and implement a method to locate submarine power cables by the magnetic field they generate.

It's assumed that the reader of this report has basic knowledge within engineering science.

Acknowledgement

I want to thank my supervisor Martin Ludvigsen for always finding time when I had pressing issues, even when his schedule was full. Further, Petter Norgen is owed a thanks for his great help regarding assembling of electronic components. Thanks is also given to Statnett SF engineer Anders Ballari for answering my many questions. Lastly, I would like to offer thanks Emil Smilden for extensive help in organising the report along with numerous coffee breaks that always made the work at hand seem more manageable.

Contents

1	Introduction	1
1.1	Motivation	1
1.2	Previous Work	2
1.2.1	Cable localisation	2
1.2.2	REMUS 100 AUV	4
1.3	Main Contributions	4
1.4	Organization of the Thesis	5
2	Theoretical Backround	7
2.1	Electromagnetism	7
2.1.1	Three-Phase Power Systems	8
2.1.2	The B-field and the H-field	8
2.1.3	Near Field and Far Field	9
2.1.4	Bessel Function	10
2.1.5	Magnetic Field around Endless Conductor	10
2.1.6	Inductance and Impedance	12
2.1.7	FEA equations	14
2.1.8	Effect of Seawater and burial	14
2.1.9	Other Observed Magnetic Fields	14
2.2	Reference Frames	15
2.2.1	NED Frame	16
2.2.2	BODY Frame	16
2.2.3	Rotation Matrix	16
2.3	Signal Processing	17
2.3.1	Fourier Analysis	17

2.3.2 LSQ curve fit	18
3 Submarine Cable Survey by Magnetometers	19
3.1 Magnetic field of Submarine AC Cables	19
3.1.1 Conductor in vacuum	20
3.1.2 Effect of metallic sheath and armour	22
3.1.3 Effect of seawater	24
3.1.4 Effect of burial	27
3.2 Cable Localisation	28
3.2.1 Single phase AC Cable	28
3.2.2 Three-Phase Power System	33
3.3 Signal processing	36
3.3.1 Isolating the cable-generated field	36
3.3.2 Calibration	36
4 Finite Element Analysis	41
4.1 Modelling	41
4.2 Finite Element Analysis Results	43
4.2.1 Magnetic Fields	43
4.2.2 Cable Localisation	48
4.2.3 Three-Phase Power System	51
4.2.4 Single cable approximation	52
4.2.5 Curve Fitting Method	53
5 Experiments	59
5.1 Equipment	59
5.2 Code	60
5.3 Marine cybernetics-laboratory	61
5.3.1 Single Phase AC Cable	61
5.3.2 Three-Phase Power System	61
5.4 Nidaros cable	62
5.4.1 Set up	63
5.5 Munkholmen cable	63
5.5.1 Set up	64

5.6 Calibration	65
5.6.1 Set up	65
6 Results	67
6.1 Marine-Cybernetic Laboratory	67
6.1.1 Single Phase AC Cable	67
6.1.2 Three-Phase Power System	69
6.2 Nidaros cable	72
6.3 Munkholmen cable	74
6.4 Calibration	75
6.4.1 Magnetometer Misalignment	75
6.4.2 Ferromagnetic Distortion	76
7 Discussion	77
7.1 Magnetic fields	77
7.2 Localisation of Single Phase AC Cables	79
7.3 Localisation of Three-Phase Power Systems	80
7.3.1 Single phase AC cable approximation	80
7.3.2 LSQ-Curve Fitting method	81
7.4 Triplex cables	82
7.5 Six single core cables	83
7.6 Calibration and misalignment compensation	83
7.7 Non-Transmitting Cables	84
8 Concluding Remarks	85
8.1 Conclusion	85
8.2 Further Work	86
Appendices	87
A Validation of FEM-modelling	89
B Single Cable Approximation	91
C Triplex Cable	93

D Ferromagnetic pipe detection	97
D.1 Intrinsic magnetisation	97
D.2 Induced Magnetic field	97
D.3 Localisation method	98
Bibliography	100

List of Figures

2.1 Current distribution in a three-phase power system	8
2.2 Magnetic field around an endless wire	11
3.1 Boundaries for induced eddy currents	26
3.2 AUV over a buried cable	29
3.3 Relative heading between AUV and cable	30
3.4 AUV and cable from above	31
3.5 AUV and cable from the front	31
3.6 Relation between direction to the cable and sign between B_z and B_y	32
3.7 The AUV's desired path along the three cables.	34
3.8 Effect of hard-iron and soft-iron distortion	37
3.9 Magnetometer and disturbances	40
4.1 Single Phase AC cable	42
4.2 AC cable buried in the soil beneath the seabed	42
4.3 B_{xy} for a single phase AC cable	43
4.4 B_z for a single phase AC cable	43
4.5 Comparison of the magnetic field between FEA and analytic models for a single phase AC cable	43
4.6 Relative strength between B_z and B_{xy} for a single phase AC cable	44
4.7 Direction of the magnetic field around a single phase AC cable	44
4.8 Magnetic flux density for a three-phase power system	45
4.9 Magnetic flux density for shielded cables in three-phase power system in air	46
4.10 Magnetic flux density for shielded cables in a three-phase power system in sea-water	46

4.11	Direction of the magnetic field around a three-phase power system	47
4.12	Cable localisation with 40cm Magnetometer spacing	49
4.13	Cable localisation 1.5m magnetometer spacing	49
4.14	Localisation of a single phase AC cable	49
4.15	Cable localisation with 40cm Magnetometer spacing	50
4.16	Cable localisation with 1.5m magnetometer spacing	50
4.17	Phase shift between B_z and B_y for a single phase AC cable	50
4.18	Cable localisation of a single phase AC cable	50
4.19	Illustration of the first FEM model	52
4.20	Single cable approximation without noise	52
4.21	Single cable approximation with noise.	52
4.22	Estimating the direction to cables in a three-phase power system	53
4.23	Curve fit of mathematical model to FEM-data	54
4.24	Curve fit of mathematical model to noise FEM-data	55
5.1	One side of the created device	60
5.2	Other side of the created device	60
5.3	Set up for experiment on a three-phase power system	62
5.4	Map of Nidaros with cables	63
5.5	Map of Korsvika with cables	64
5.6	Munkholmen Cable	64
5.7	REMUS 100 AUV and magnetometer module	65
6.1	Relative phase between B_z and B_y with respect to the horizontal distance	67
6.2	Relative heading between the AUV and the cable	67
6.3	Estimated and true distance to a single phase AC cable	68
6.4	Direction to the cable by the posterior probability function	69
6.5	Curve fitting of Biot-Savart law to measurements of B_{xy}	70
6.6	Curve fitting of Biot-Savart law to measurements of B_z	70
6.7	Measurement of the magnetic field at Nidaros	72
6.8	Magnetic flux density B_{tot} directly above the cables at Nidaros.	72
6.9	Magnetic flux density B_{tot} when 5m to the side of the cables at Nidaros.	73
6.10	Magnetic field of Munkholmen cable	74

6.11 Misalignment compensation results	75
6.12 Ferromagnetic calibration results	76
A.1 Layout of a single phase AC cable	89
A.2 Comparison of FEM models	90
B.1 Cable localisation when crossing over cables with 30 meter spacing	91
B.2 Outcrop of the leftmost cable	91
C.1 Single Phase AC cable	93
C.2 Magnetic field of non-twisted triplex cable	94
C.3 Direction of the field from non-twisted triplex cable	95
D.1 A pipe, the AUV and two magnetometers in a gradiometer setup	99

List of Tables

4.1	Cable localisation by LSQ curve fitting	54
4.2	Cable Localisation by LSQ curve fitting to noisy FEM-data	56
6.1	Cable Localisation by LSQ curve fitting to measurmeents	71

Chapter 1

Introduction

An extensive network of conductors is needed to transmit electricity from power stations to the consumers. The conductors can either be airborne and attached to great masts, or isolated and buried underground.

When the conductors are crossing large portions of water, they are generally buried beneath the seabed as underground power lines. There are mainly three different ways to transmit electricity in underwater power lines: As one conductor in a cable transmitting direct current (DC), as three alternating currents (AC) fit into the same cable, or as three alternating currents where each conductor is in a separate cable. The two latter are the main concern of this thesis.

The AC cables are generally more effective than their DC counterparts for distances less than 100km [35] and are therefore extensively used under Norwegian fjords and from the mainland to coastal islands. Installed cables need to be maintained, while new projects are ongoing to meet the demand of the consumers. To keep up with the expanding submarine power grid [2] new, and more effective, survey methods are needed.

1.1 Motivation

Statnett SF is the system operator for the Norwegian energy system. They install and maintain several underwater AC power lines throughout Norway. These submarine cables are vulnerable to environmental damages and human activities; e.g. turbulent currents, an-

choring and trawl-nets [19, 17, 36]. To prevent this type of damage the cables are usually buried.

A part of maintaining the cables is to carry out underwater surveys. These surveys should ensure that the cables are properly buried, and inspect for signs of damage. In a survey, submarine cables are located with payload sensors, such as: side-scan sonars, underwater cameras, and magnetometers. For detection of cables that are periodically buried and produce a magnetic field the most convenient sensors are magnetometers [36, 37]. This is especially true for telecommunication cables, which are relatively thin and difficult to locate with acoustic or visual methods [36].

Today, Statnett SF uses Remote Operated Vehicles (ROVs) deployed with a camera to survey their cables. This is both tedious and expensive. This follows from ROVs traditionally being slower than their Autonomous Underwater Vehicle (AUV) counterpart, and that a full crew, with a sizeable vessel, is needed to operate most ROVs. Potentially, a fully autonomous survey by AUVs could significantly reduce the cost and time of survey operations. Particularly because Statnett's AC cables produce a powerful magnetic field, which can be located and tracked by magnetometers [34]. Effectively, this removes the need of a human operator manually controlling the vehicle by a video stream.

Statnett SF initiated this thesis to review, design, and implement methods for submarine AC cable localisation by magnetometers. Another thesis was initiated in conjunction with this and regards designing and implementing control systems for cable tracking on Remus 100 AUV. Together they should, ideally, carry out an AUV-based submarine cable survey by magnetic-based cable tracking.

1.2 Previous Work

1.2.1 Cable localisation

The first transatlantic optical fibre cable was installed in 1988 and already in 1994 an AUV-based survey was carried out on a submarine cable [36, 19]. The AUV was deployed with a camera and two magnetometers and successfully tracked along a telecommunication cable outside of Hokkaido, Japan. Today, over 850 000km of submarine cables spans the earth

[31]. Naturally, several survey methods have been developed to maintain these. The general methods are Sonar-Based, Visual-Based, and Magnetic-Based. The methods are not mutually exclusive, and commercial products often use a combination [12]. The magnetic based methods are divided into two subgroups:

Active methods use an electric pulse to induce eddy currents in ferromagnetic materials. The object of interest can then be located by the magnetic field of the induced eddy current by on-board magnetometers. Active methods are mostly used on ferromagnetic material like undetonated mines and pipes not conducting electricity [12]. Passive methods detects submarine transmission lines by the magnetic field produced by the alternating current. For AC-power lines the field is strong enough to be detected as is [34], while a tone can be applied to telecommunications cable to detect these as well. The later requires onshore access to the line so a current can be applied [36].

Passive methods, and active methods, uses the same techniques to locate the object from the magnetic field. By not needing equipment to induce pulses passive methods are generally cheaper and easier to implement[12]. This make them the clear choice for AC-power cables.

SmartTrack by Innovatum and **Orion** by Optimal ranging are commercial products which has implemented passive methods for cable localisation. Both products use, at least, two tri-axial magnetometers and locates the cable by triangulation of the magnetic amplitude in each axis [12] [24]. A detailed derivation of a triangulation method to locate an AC-cable is published in Sensors Open Acess Journals [36], and from the multi-axis, multi-magnetometer set up it is fair to assume that Orion and SmartTrack use the same underlying equations. This follows from there only being one way to triangulate the magnetic amplitudes to locate a cable. Actually, the same argument can be used for the survey carried out in Japan in 1994 [19] such that the underlying equation seems to be dating at least this far back. Naturally, AUVs and magnetometers have made significant technological advances since that time, and the calibration and prepossessing routines is different for each system.

1.2.2 REMUS 100 AUV

In this thesis, submarine cable survey methods are designed with respect with the available sensors, and limitations, of REMUS 100 AUV. A detailed article of REMUS 100 AUV's configurations and payload sensors are given in [22], and their applicability for magnetic-based cable survey are presented in the preliminary work to this thesis by the same author [14]. A full presentation will not be restated here, but generally, the relevant payload sensors are a Side-Scan-Sonar, to acoustically scan the seabed; an Acoustic Doppler Current Profiler (ADCP), to estimate the vehicle's velocity, position and distance to the seabed; a magnetic compass, to measure the vehicle's heading; and a gyroscope, to determine the AUV's orientation.

1.3 Main Contributions

Localisation, and tracking, of a single submarine AC cable has been widely researched and implemented [36, 12, 24]. However, the challenges arising with three-phase power systems complex magnetic field have not been explicitly tackled. SmartTrack is able to locate a cable in a three-phase power system, but only if the other cables are not too close [12]. In this thesis, cable localisation, and tracking, of AC cables in a three-phase power system is explored. Generally, the main contributions can be divided into three parts: design, simulations, and experiments.

Design: A mathematical model has been derived that describes the magnetic field around three single-core cables in a three-phase power system. This method includes both the effect of cable shields and seawater. This mathematical model is used to design a cable tracking, and localisation, method for cables in a three-phase power system. For single AC cables a method is established that can find the direction to it at a greater distance than existing methods. Also, some light is shed on when the other cables in a three-phase power system are too close for using existing methods. Lastly, routines to calibrate magnetometers on Remus 100 AUV have been established, and a method is formulated that transforms the cables' locations to a global reference frame.

Simulations: Finite Element Models were created to simulate a magnetic field equivalent to that around AC power lines. Models were created for both a single cable and cables in a three-phase power system. The established methods for cable localisation were tested on the simulated magnetic field obtained from this analysis.

Experiments: A device has been made for implementation of magnetic-based cable localisation on REMUS 100 AUV. The device consist of a mini-computer, a digital-to-analogue converter and two magnetometers. Experiments have been carried out with this device. The experiments includes cable localisation of both a single low-voltage AC conductor and three low-voltage conductors in a three-phase power system. Finally, the calibration routines have been implemented and tested on Remus 100 AUV.

1.4 Organization of the Thesis

This thesis starts in **Chapter 2** by presenting theory regarding electromagnetism, reference frames, and signal processing that is needed for magnetic-based cable survey. This theory is applied in **Chapter 3** to derive an expression for the magnetic field around shielded cables in seawater, formulate cable localisation methods, and to establish routines for calibration of the magnetometers. In **Chapter 4** Finite Element Models are created both for a single cable and cables in a three-phase system. Analysis are carried out on said models and the methods are tested on the magnetic field obtained. The results from this simulation is given at the end of the same chapter. Further, **Chapter 5** presents the experiments carried out and **Chapter 6** shows the results from these. Lastly, a discussion of the results are given in **Chapter 7**, before the thesis is concluded in **Chapter 8**.

Chapter 2

Theoretical Background

This chapter is based on the same chapter written in the preliminary work to this thesis by the same author [14]. It starts with a brief introduction in electromagnetism before the relevant magnetic fields for an AUV on a survey are presented. Thereafter, the different coordinate frames used are explained along with the transformation between these. Finally, theory needed for successfully processing the magnetic field signal is given.

2.1 Electromagnetism

"Magnetism is nothing more than electrostatics combined with special relativity" [25]. It is not expected that readers know the workings of special relativity but in layman's terms it means that distance (and time) changes with the point of reference.

For example, if a point charge is moving upwards and a wire to the side has a current downwards they will exert an electrostatic force on each other. However if the frame is changed to the moving point charge the electrons in the wire will seem closer together and therefore the net electrostatic force will be greater than viewed from an external *labframe*. Thus instead of changing the frame back and forth between charges a pure mathematical force is introduced. This is called the magnetic force and allows for calculations in only one frame¹.

¹This is a simplification

2.1.1 Three-Phase Power Systems

In a three-phase power system the three currents are, ideally, 120° phase shifted to each other. As a direct consequence the net current is zero at all times. Compared to an AC system using two conductors a three-phase power system transmits three times the energy [34]. That is, the energy per conductor is doubled. This system is therefore widely used for high-voltages cables. An illustration of the current distribution can be seen in Figure 2.1. The current in a three-phase power system can be given in several ways. In this thesis it's given by its root mean squared value (RMS), which is

$$I_{RMS} = \frac{I_{max}}{\sqrt{2}} \quad (2.1)$$

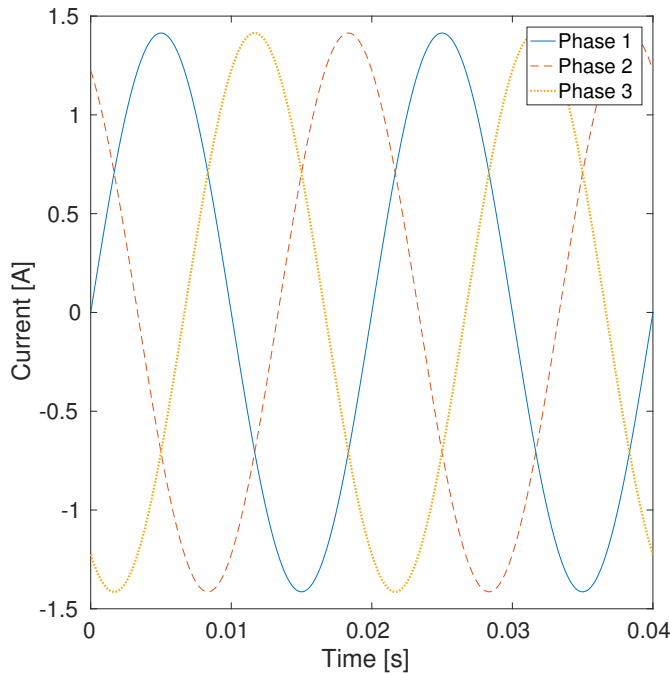


Figure 2.1: The current of the three phases in a three-phase power system with a frequency of $f = 50\text{Hz}$ and current of $I_{RMS} = 1[\text{A}]$

2.1.2 The B-field and the H-field

It is often distinguished between two field representations of the *Magnetic field*. The *H* field is the historical definition of the magnetic field and given in Amperes/meter [7]. That is, the

charge per second per relative velocity. The B field, measured in Tesla, is proportional to this field but is defined to fulfil the Lorentz force law on a particle.

$$\mathbf{F} = q(\mathbf{E} + \mathbf{v} \times \mathbf{B}) \quad (2.2)$$

q is the particle charge, E the electric field and v the velocity of the particle.

The B field therefore corresponds to the magnetic flux inside a given material and differs from H by the constant magnetic permeability μ of the given material. A magnetometer will measure the B field and this field is therefore be the main concern of this thesis. To prevent confusion the B field is from this point onward denoted as the magnetic field, or the magnetic flux density. The H field is denoted as the *magnetising field*.

2.1.3 Near Field and Far Field

The characteristics of the magnetic field greatly differs with the distance from the source. As a rule of thumb, the near field is within one wavelength. [34]². In the far field, the solution of Maxwell's equations leads to electromagnetic waves that dissipates through space. For the near field, however, the electric and magnetic field is approximately independent. Also, in the near field the magnetic field builds up and retracts almost without energy leaving the source. This is called a reactive field and the practical consequence of this is that the field around an endless wire reduces proportional to r^{-1} instead of a higher order. Another effect is that the field cannot be modelled as EM waves. This makes it difficult to derive an expression for propagation through conductive material.

For a 50Hz cable, the near field is within a radius of

$$\lambda = \frac{c}{f} = \frac{30 * 10^8 \text{ m/s}}{50 \text{ Hz}} = 600 \text{ km} \quad (2.3)$$

And the reactive field is within

$$\text{Reactive Field} = \frac{\lambda}{2\pi} = 95.5 \text{ km} \quad (2.4)$$

It is safe to assume a reactive field, and by extension, a near field which makes equation (2.7)

²Actually, it's a gradual change between then near and far field

valid for cable localisation at this frequency.

2.1.4 Bessel Function

Bessel functions are solutions to the differential equation

$$x^2 \frac{d^2 y}{dx^2} + x \frac{dy}{dx} + (x^2 - \alpha^2) y = 0 \quad (2.5)$$

The solution is dependent on the boundary set at the origin. The different solutions are denoted as the Bessel function of first, second or third kind. Further, if α is an integer this integer denotes the order of the solution. Further, the solution is always harmonic and appears when finding solutions for the Laplace equation in cylindrical coordinates. It is therefore important for many problems involving radial propagation of electromagnetic waves.

Modified Bessel functions are solutions of

$$x^2 \frac{d^2 y}{dx^2} + x \frac{dy}{dx} - (x^2 - \alpha^2) y = 0 \quad (2.6)$$

Where α is a complex number. The solution is here not harmonic, but exponentially increasing or decaying. Thus, instead of describing the EM wave at time (t) as the Bessel functions, the modified Bessel functions may be used to describe the decay of the peak field.

2.1.5 Magnetic Field around Endless Conductor

One Conductor

For an endless wire the field is a specific solution of Ampere's Law given by

$$B = \frac{\mu_0 \mu_r I}{2\pi r} \quad (2.7)$$

I is the current, and r the distance to the wire. $\mu_0 [\frac{\text{Newton}}{\text{Ampere}^2}]$ is the vacuum permeability and μ_r is the relative permeability of the material that contains the wire. The direction of the field is given by the right-hand-rule.

For an AC current the magnetic field will oscillate with the same frequency, and proportional strength, to the current. The magnetic field can be written as

$$B(t, r) = \frac{\mu_0 I_0 e^{i(\omega t + \phi)}}{2\pi r} \quad (2.8)$$

For two parallel wires the magnetic force is orthogonal to each other and we can therefore use superposition to get the total contribution.

$$B_{tot} = \frac{\mu_0 I_1}{2\pi r_1} \pm \frac{\mu_0 I_2}{2\pi r_2} \quad (2.9)$$

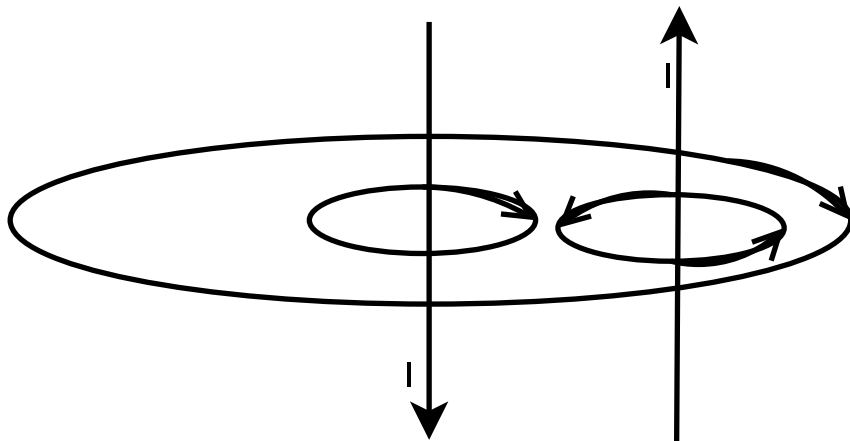


Figure 2.2: Magnetic field around two endless wires note the field is amplified between the cables and countered outside

Three-Phase Power System

Three-phase systems are used because more energy can be transported per conductor area. The magnetic field around a three-phase current is a special case of the current around three parallel wires. In a three-phase power system there are three AC conductors all having the same frequency and, ideally, same amplitude. The currents are phase-shifted with 120° to each other making the net current zero at all times. The magnetic field produced from each is

$$B(r, t) = \frac{\mu_0 \mu_r I_0 e^{i(\omega t + \phi_k)}}{2\pi r} \quad (2.10)$$

Where ϕ_k is the phase shift for the cable in question.

The superposition of the field from all cables is *elliptically polarised* [34]. This means that

both its strength and direction will change in time. Actually, the field vector will draw an ellipsoid in a plane orthogonal to the cable's direction [34]. This follows from the vector of the tree fields not pointing in the same direction. It is therefore more intuitive to represent the total field in its X and Y component.

$$B(r, t)_x = \frac{u_0 I_0 e^{i(\omega t + \phi_k)}}{2\pi r} \frac{y_l - y}{r} \quad (2.11)$$

$$B(r, t)_y = \frac{u_0 I_0 e^{i(\omega t + \phi_k)}}{2\pi r} \frac{x_l - x}{r} \quad (2.12)$$

The total field components are attained by adding the components from all he three phases. A more thorough derivation of the peak magnetic field of a three-phase power system is given in chapter 3.

2.1.6 Inductance and Impedance

"In electromagnetism and electronics, **inductance** is the property of an electrical conductor by which a change in current through it induces an electromotive force in both the conductor itself and in any nearby conductors by mutual inductance". [26]

In other words, if an alternating current is present in a conductor it will produce an alternating magnetic field. This time-varying magnetic force will induce a current in nearby conductors.

For a three-phase power system the nearby conductors are each of the three phases, and also the metallic sheath and armour covering the inner conductors. The cables can be assumed as parallel wires and their inductance is then the sum of the magnetic flux between the wires per current in them. [13].

$$L = \frac{\mu_0}{2\pi} \int_{r_c}^d \frac{1}{r} dr \quad (2.13)$$

d is the distance between the wires and r_c is the conductor radius.

For three conductors in a three-phase system with an arbitrary formation the inductance is:

([23])

$$L_1 = \frac{\mu_0}{2\pi} \ln\left(\frac{1}{r_c}\right) + a^2 \ln\left(\frac{1}{D_{12}}\right) + a \ln\left(\frac{1}{D_{13}}\right) \quad (2.14)$$

$$L_2 = \frac{\mu_0}{2\pi} \ln\left(\frac{1}{r_c}\right) + a^2 \ln\left(\frac{1}{D_{12}}\right) + a \ln\left(\frac{1}{D_{23}}\right) \quad (2.15)$$

$$L_3 = \frac{\mu_0}{2\pi} \ln\left(\frac{1}{r_c}\right) + a^2 \ln\left(\frac{1}{D_{23}}\right) + a \ln\left(\frac{1}{D_{13}}\right) \quad (2.16)$$

(2.17)

Where $D_n k$ are the distances between the cables, r_c is the radius of the conductor and $a = \frac{1}{2} - 1i\frac{\sqrt{3}}{2}$. As already stated, the inductance is the magnetic flux per current. The purpose of a is therefore to compensate for the different phases in the three currents.

Impedance is the AC equivalent of DC resistance. In a DC the resistance of a conductor affects the current with a relation known as Ohm's law

$$V = \frac{I}{R} \quad (2.18)$$

V is the voltage, $I[A]$ the current and $R[\Omega]$ the resistance. The impedance is made up from two terms. The resistance, which affects the amplitude, and the reactance, which affect the phase. The equation for impedance is

$$Z = R + i * \omega * L \quad (2.19)$$

$\omega [rad]$ the angular frequency of the current field and $L [Henry]$ is the inductance of the conductor. The inductance times the angular frequency is often denoted as the reactance.

$$X = \omega L \quad (2.20)$$

Ohm's law is also valid for alternating currents and is

$$V = \frac{I}{Z} \quad (2.21)$$

Actually, Ohms law for DC is only a special case with $X = 0$. For a transmission line both L and R are usually given as per meter wire for the cross-section in question.

2.1.7 FEA equations

The FEA(Finite Element Analysis) program used for this thesis is Comsol AC/DC module TM. For solving for the magnetic field Comsol use Maxwell's equations ((2.22)) [9].

$$\nabla \cdot D = \rho \quad \nabla \times E = -\delta_t B \quad (2.22)$$

$$\nabla \cdot B = 0 \quad \nabla \times H = J + \delta_t D \quad (2.23)$$

Where ρ is the electric charge density, E is the electric field, D the electric displacement field, J the current density, H the magnetising field, and B the magnetic flux density.

In this thesis it is desired to know the magnetic flux density B [Tesla] as this is the field measured by a magnetometer. To solve Maxwell's equations boundary conditions are needed.

For a known frequency Comsol uses the magnetic field interface

$$\nabla \mu^{-1}(\nabla \times A) + (j\omega\sigma - \omega^2\epsilon)A = J_s \quad (2.24)$$

Here, μ is the magnetic permeability, A the magnetic vector potential, ω is the frequency of the field, σ the conductivity of the material and ϵ the permittivity. The magnetic flux is given as $B = \nabla \times A$. Thus by numerically solving Eq. 2.24 for the given mesh B is obtained.

2.1.8 Effect of Seawater and burial

Seawater is conductive and the soil might be. An alternating magnetic field will induce eddy currents in conductive materials. The effect from this is that the magnetic field will lose magnitude and get a phase lag. Effectively, the soil and seawater can be seen as having impedance's to the magnetic field. A more thorough derivation of the effect of seawater and burial will be presented in chapter 3.

2.1.9 Other Observed Magnetic Fields

When the AUV moves through space its magnetometers will register a varying magnetic field. This magnetic field is caused by a number of different sources. In this section, the most

important are listed.

The Geomagnetic Field

This field is the earth induced field used for navigation with your everyday compass. The field is believed to be induced by the Earth's iron core and has a strength dependent on where you are on Earth. In Norway it has both a vertical and an horizontal component and a strength of about $50\mu\text{T}$.

The Vehicle-Induced Field

This field is generated by ferromagnetic material and electronics on board AUV REMUS. The main collaborator is the engine which has a DC current. However, since the thrust is dependent on the navigation and orientation, the magnetic field will vary. The reach of this field is very short and can be minimised by moving the sensors away. Also, some of it should be filtered out by the initial calibration loop.

The Cables Magnetic Field

The field of interest in this thesis. It will have a frequency of 50Hz and decay proportionally with the distance to the cable.

Anomaly Field

The Anomaly field is caused by local magnetised rocks and substances. It might be natural like basalt, or from ferromagnetic pipes and cables. It is characterised by a relatively small wavelength and has therefore a short reach[15].

2.2 Reference Frames

When detecting a cable, it is desired to know its position, its direction, as well as its depth below the seabed. In this thesis, two reference frames are used.

2.2.1 NED Frame

This frame is used for day to day navigation. Its origin is fixed on a point on the earth's surface and the axes points North, East, and Down . Using the NED frame is often called "flat-earth-navigation" as it assumed a tangential plane where the origin touches the earth's surface. The cable's position should be given in this frame.

2.2.2 BODY Frame

This frame is fixed on the vehicle and moves with it. The axes x,y,z follows the SNAME convention and are the length, the width and the thickness of the vehicle. The NED frame should describe the position and orientation of the craft, while linear and angular velocities should be given in the BODY frame.[32]

2.2.3 Rotation Matrix

When REMUS 100 AUV is moving in the magnetic field its magnetometers will observe the magnetic field relative to its BODY-frame. To transform this to the NED-frame, Euler angles and the Rotation matrix are introduced. Because REMUS supplies the attitude data it is only necessary to know the BODY-to-NED rotation matrix [32].

$$R(\Theta_{nb}^b) = \begin{bmatrix} c\psi c\theta & -s\psi c\phi + c\psi s\theta s\phi & s\psi s\phi + c\psi c\phi s\theta \\ s\psi c\theta & c\psi c\phi + s\phi s\theta s\psi & -c\psi s\phi + s\theta s\psi c\phi \\ -s\theta & c\theta s\phi & c\theta c\phi \end{bmatrix} \quad (2.25)$$

The magnetic field is then given by

$$M^n = R(\Theta_{nb}^b) M^b \quad (2.26)$$

Where M^n and M^b is the magnetic field in NED and BODY-frame respectively.

The roll ϕ and pitch θ angles can be found by a gyroscope and the yaw angle ψ from the magnetic compass. Both of which are present on the REMUS 100 AUV[22].

2.3 Signal Processing

The detected magnetic field will be a combination of all the observed magnetic fields. To locate the cable it's necessary to isolate the magnetic field it generates.

2.3.1 Fourier Analysis

The Discrete Fourier Transform (DFT) is given by

$$X_k = \sum_{n=0}^{N-1} x_n e^{-\frac{2\pi i}{N} nk} \quad (2.27)$$

$$= \sum_{n=0}^{N-1} x_n \cdot (\cos(-2\pi k \frac{n}{N}) + i \sin(-2\pi k \frac{n}{N})) \quad (2.28)$$

Here N as the number of samples, n is the current sample, x_n is the samples value and X_k is a complex number that represents the magnitude and phase for the frequency given by index k .

The (DFT) decomposes a signal into its frequency parts [16]. It does this by calculating the covariance between the sampled signal and an imaginary signal with a frequency between zero and the sampling frequency. If the absolute value of the covariance is high there exists much of this frequency in the sampled signal.

After using the DFT on a set of samples the index corresponding to a given frequency can be found by

$$k = \frac{N}{f_s} f_o \quad (2.29)$$

Where k is the index, f_s the sampling rate, and f_o is the frequency of the original signal. Reconstructing the original amplitude from the signal is a bit more complex and involves normalising the Fourier transform. For frequencies beneath the Nyquist Frequency $f_n = 0.5f_s$ this is generally given as

$$A = \text{abs}(X_k(k)) \cdot \frac{2}{N} \quad (2.30)$$

The magnitude per samples is multiplied by two to account for the symmetrical folding around the Nyquist Frequency. If the frequency of interest is the Nyquist Frequency the magnitude does not need to be multiplied by two.

Fast Fourier Transform

The Fast Fourier Transform (FFT) is a set of computer algorithms that dramatically speeds up the time used to find the discrete Fourier transform [18]. This is possible as many of the calculations in the DFT are repeated. There are many different FFTs algorithms, but the most common algorithm and the one that is used in this thesis is the radix-2 Cooley–Tukey algorithm. Cooley-Turkeys algorithm works by dividing the DFT problem into smaller DFT problems and solving for each one [18]. The radix-2 method is more specific and divides the DFT into an odd and an even part. This requires the number of samples to be an even multiple of 2. This is easily obtained as the number of samples can be chosen. Effectively the algorithm turns (2.27) into

$$X_k = \sum_{m=0}^{N/2-1} x_{2m} e^{-\frac{2\pi i}{N}(2mk)} + \sum_{m=0}^{N/2-1} x_{2(m+1)} e^{-\frac{2\pi i}{N}(2(m+1)k)} \quad (2.31)$$

An effectively implemented FFT algorithm is a magnitude of 1000 times faster than directly solving the DFT formula [33]. Most major programming languages like Python and C++ have implemented FFT libraries that can be downloaded and used as is.

2.3.2 LSQ curve fit

Least Squared Curve fitting tunes parameters to minimise the function

$$z = \min \left(\sum_{n=1}^{n=N} (y_i - f(x_i, \beta)) \right) \quad (2.32)$$

Where y_i are some measurements $f()$ is a mathematical model of the system being measured, x_i is the independent variable and β are a set of variables being tuned to minimise Eq. (2.32).

Chapter 3

Submarine Cable Survey by Magnetometers

In this chapter, the theory that was introduced in the previous is used to describe the steps needed to fulfil a cable survey with magnetometers. This chapter starts by a derivation of a mathematical model to describe the magnetic field about both a single-phase cable and cables in a three-phase power system. Further, cable location techniques are presented for both cases. Lastly, the signal processing required to get usable magnetometer data is given. This includes a calibration routine and compensating for misaligned sensors.

3.1 Magnetic field of Submarine AC Cables

As previously mentioned, the AUV will always be in the vicinity of the cables' near-field. This follows from the wavelength being in same ballpark as the earth's diameter ([34]). An effect of this is that the magnetic field does not propagate as electromagnetic (EM) waves. This makes it difficult to find an analytic solution of the magnetic field when it passes through a conductive medium. This section starts with the basic equation for the magnetic field around an endless conductor and extends this to find the peak magnetic field for both a single phase AC cable and for cables in a three-phase power system. Further, an equation is derived that estimates the effect of metal shield and armour on three-phase power systems, before the effect of seawater is formulated. Combining all these parts gives a mathematical

model of the magnetic field when flying over a three-phase power system in seawater.

3.1.1 Conductor in vacuum

By assuming and endless cable the magnetic field can be approximated by superposition of Biot-Savart law (Eq. (2.7)) From this, the total magnetic field from n endless conductors is:

$$B_{tot_z} e^{i(\omega t + \chi_1)} = \left(\frac{K}{(XY)_1^2 + Z_1^2} (XY)_1 e^{i(\omega t + \phi_1)} \dots + \frac{K}{(XY)_n^2 + Z_n^2} (XY)_n e^{i(\omega t + \phi_n)} \right) \quad (3.1)$$

$$B_{tot_{xy}} e^{i(\omega t + \chi_2)} = \left(\frac{K}{(XY)_1^2 + Z_1^2} Z_1 e^{i(\omega t + \phi_1)} \dots + \frac{K}{(XY)_n^2 + Z_n^2} Z_n e^{i(\omega t + \phi_n)} \right) \quad (3.2)$$

Where $K = \mu_0 * I / (2\pi r)$, I is a complex number representing the current magnitude and phase, and μ_0 is the vacuum permeability. XY is the combination of the AUV's X and Y axis and is used throughout this thesis to simplify equations to 2D while taking into account that the AUV's axis isn't necessarily aligned with the cable's.

For simplicity $\frac{K(XY)_k}{(XY)_k^2 + Z_k^2}$ is rewritten as B_{zk} . Same goes for the XY axis. Assuming equal frequency for all conductors and multiplying equation (3.2) with $e^{-i\omega t}$ gives

$$B_{z_{tot}} e^{i\chi_1} = B_{z1} e^{i(\phi_1)} \dots + B_{zn} e^{i(\phi_n)} \quad (3.3)$$

$$B_{xy_{tot}} e^{i\chi_2} = B(xy)_1 e^{i(\phi_1)} \dots + B(xy)_n e^{i(\phi_n)} \quad (3.4)$$

Now, the peak can be found for all cases by the complex absolute value ([10]), which is far simpler than to differentiate and find the max with respect to the time t .

Single Phase AC cable

This case is not commonly used to transmit electricity, the only real case would be if the seawater was used as the return current. Other, more realistic, cases is using this as a simplification when the return current(s) is(are) far away.

For a single cable the field is Biot-Savarts law as given in equation (2.7).

$$\begin{aligned} B_{xy} &= c \cdot \frac{\mu_0 * \mu_r * I * (z_l - z)}{2 * \pi * r^2} \\ B_z &= c \cdot \frac{\mu_0 * \mu_r * I * ((xy)_l - xy)}{2 * \pi * r^2} \end{aligned} \quad (3.5)$$

Where c is a constant to compensate for unmodeled effects, e.g.; seawater and magnetic shields, and $z_l, (xy)_l$ are the vertical and horizontal location of the cable.

As there is only one source the magnetic field will have its peak and B_{xy} and B_z at the same time and the total field perpendicular to the direction of the cable.

Three-Phase Power System

Multiple phase shifted harmonic functions of same frequency will make it's own harmonic function with the same frequency, but phase shifted to all. As there are infinite ways this harmonic function can be created it's not trivial to decompose it to its individual phase parts.

For multiple cables the magnetic field from each will combine into a magnetic field which varies greatly from every point in space. Each of these fields points in different directions depending on the position of the cables. It is therefore necessary to decompose the fields into z and xy components and find the peak for each. This peak is given by the complex value of Eq. (3.4). For a three-phase system the complex absolute value is

$$\begin{aligned} |(B_{z_{tot}} * e^{\omega t + \chi})|^2 &= |B_{z_1} e^{\omega t} + B_{z_2} e^{\omega t + \phi_1} + B_{z_3} e^{\omega t + \phi_2}|^2 \\ |B_{z_{tot}} e^\chi|^2 &= |B_{z_1} + B_{z_2} e^{\phi_1} + B_{z_3} e^{\phi_2}|^2 \\ B_{z_{tot}}^2 &= (B_{z_1} + B_{z_2} \cos(\phi_1) + B_{z_3} \cos(\phi_2))^2 + (B_{z_2} \sin(\phi_1) + B_{z_3} \sin(\phi_2))^2 \\ &= B_{z_1}^2 + B_{z_2}^2 + B_{z_3}^2 + 2E_{z_1} B_{z_2} \cos(\phi_1) + 2E_{z_1} B_{z_3} \cos(\phi_2) \\ &\quad + 2E_{z_2} B_{z_3} \cos(\phi_1) \cos(\phi_2) + 2E_{z_2} B_{z_3} \sin(\phi_1) \sin(\phi_2) \end{aligned} \quad (3.6)$$

For a three-phase system with $\phi_1 = 120$ and $\phi_2 = 240$ this reduces to

$$B_{z_{tot}} = \sqrt{B_{z_1}^2 + B_{z_2}^2 + B_{z_3}^2 - B_{z_1} B_{z_2} - B_{z_1} B_{z_3} - B_{z_2} B_{z_3}} \quad (3.7)$$

The exact same derivation is naturally valid for $B_{xy,tot}$ and the magnetic flux density norm is

$$B_{tot} = \sqrt{B_{z,tot}^2 + B_{xy,tot}^2} \quad (3.8)$$

The total field B_{tot} should be seen as a mathematical description and not as an actual physical phenomenon. This follows from that from multiple sources, not located in the same place, the peak of B_{xy} and B_z will not necessarily occur at the same time. Actually, it will only very rarely do so.

3.1.2 Effect of metallic sheath and armour

Eddy currents are induced in the sheath and armour, this affects the overall magnetic field. If the armour and sheath is grounded at only one end, eddy currents and currents from capacitance will occur. However, if they are bound at both ends a circulation current is induced. This is often referred to as *solid bonding* and is the standard on submarine cables [6, 3]. If the sheath and armour is solid bonded the the out of plane (along cable) circulation currents are much greater than the radially eddy currents and currents from capacitance, and they can be neglected [1, 6, 13].

It's desired to derive an expression for the induced circulating currents in the armour and the sheath. This follows from this current will also produce a magnetic field, that generally negates that of the inner conductor [1]. The relation between voltages and currents in the conductor, sheath and armour is given by Ohm's law

$$\begin{Bmatrix} V_c \\ V_s \\ V_a \end{Bmatrix} = \begin{Bmatrix} Z_{cc} & Z_{cs} & Z_{ca} \\ Z_{sc} & Z_{ss} & Z_{sa} \\ Z_{ac} & Z_{as} & Z_{aa} \end{Bmatrix} \begin{Bmatrix} I_c \\ I_s \\ I_a \end{Bmatrix} \quad (3.9)$$

Where c, s, a is the conductor, sheath and armour respectively, and V, Z, I are the voltages impedances and currents. Explicitly Z_{sc} is the impedance in the sheath as a form of its own conductor and the conductors in other cables.

In [13] a thorough derivation is presented regarding the impedance's for three cables with armours and sheaths in a trefoil formation. That is, all the cables are equally spaced as corners of a triangle. The sheath-sheath and sheath-conductor internal and mutual inductance are

here given as¹.

$$L_{cs} \approx L_{ss} \approx \frac{\mu_0}{2\pi} \ln\left(\frac{s}{r_s}\right) + \frac{\mu_0 t_a}{2\pi r_a} [\mu_t \cos^2(\beta) - 1] + \frac{\mu_0 \mu_e A_a}{2\pi r_a l_a} \quad (3.10)$$

s is the axial distance between the cables and r_s is the radius of the sheath. The second term is the effect from a magnetic armour and the last is for the *helical lay*² of the armour wires. The two latter terms are depended on the distance for between a full revolution of the armour wire l_a and the longitudinal magnetic permeability μ_e . The two latter terms are not depended on the relative location of the cables and are therefore internal inductance terms. By neglecting them Eq. (3.10) reduces to the basic inductance of a trefoil formation $L_{cs} = \frac{\mu_0}{2\pi} \ln\left(\frac{s}{r_s}\right)$, which is the sum of the internal and mutual inductance. For an asymmetrical formation the same inductance is given as [23]

$$L_1 = \frac{\mu_0}{2\pi} \ln\left(\frac{1}{r_{sa}}\right) + a^2 \ln\left(\frac{1}{D_{12}}\right) + a \ln\left(\frac{1}{D_{13}}\right) \quad (3.11)$$

$$L_2 = \frac{\mu_0}{2\pi} \ln\left(\frac{1}{r_{sa}}\right) + a^2 \ln\left(\frac{1}{D_{12}}\right) + a \ln\left(\frac{1}{D_{23}}\right) \quad (3.12)$$

$$L_3 = \frac{\mu_0}{2\pi} \ln\left(\frac{1}{r_{sa}}\right) + a^2 \ln\left(\frac{1}{D_{23}}\right) + a \ln\left(\frac{1}{D_{13}}\right) \quad (3.13)$$

$$(3.14)$$

Where $D_n k$ are the distances between the cables and $a = \frac{1}{2} - 1 i \frac{\sqrt{3}}{2}$ Inserting this inductance into Eq. (3.10) gives the total inductance as

$$L_{cs_k} \approx L_{ss_k} = L_k + \frac{\mu_0 t_a}{2\pi r_a} [\mu_t \cos^2(\beta) - 1] + \frac{\mu_0 \mu_e A_a}{2\pi r_a l_a} \quad (3.15)$$

This is valid because the latter terms are internal properties of each cable. A simplification, as presented in [5], is to assume the armour and sheath is connected in parallel. They then share a common resistivity $R_e = (\frac{1}{R_s} + \frac{1}{R_a})^{-1}$. Further, the impedance is

$$Z = R_e + i X_k \quad (3.16)$$

X_k is the reacatance given as

$$X_k = \omega L_k \quad (3.17)$$

¹A small simplification is introduced negating the armour thickness as it is much smaller than armour radius

²The armour wires are twisted around the cables to reduce the circulating current induced in them

With this Eq. (3.9) can be written as

$$V_{sa} = (I_{sa} + R_e) + (I_c + I_{sa}) * i\omega L_{cs} \quad (3.18)$$

As the cables are grounded at both ends a circulating current flows and the voltage difference in zero. From Eq. (3.9) the sheath and armour currents in the sheath-armour for each cable then becomes

$$I_{sa} = \frac{-I_c i\omega L_{ss}}{(R_e + i\omega L_{ss})} \quad (3.19)$$

$$= \frac{-I_c \omega (iL_k + i \frac{\mu_0 t_{sa}}{2\pi r_{sa}} [\mu_t \cos^2(\beta) - 1] + i \frac{\mu_0 |\mu_e| A_a \sin(\beta) \cos(\gamma)}{2\pi r_a l_a} + \frac{\mu_0 |\mu_e| A_a \sin(\gamma) \cos(\beta)}{2\pi r_{sa} l_{sa}})}{R_e + \frac{\omega \mu_0 |\mu_e| A_a \sin(\gamma) \cos(\beta)}{2\pi r_{sa} l_{sa}} + \omega i L_k + \omega i \frac{\mu_0 t_{sa}}{2\pi r_{sa}} [\mu_t \cos^2(\beta) - 1] + \omega i \frac{\mu_0 |\mu_e| A_a \sin(\beta) \cos(\gamma)}{2\pi r_a l_a}} \quad (3.20)$$

Where A_a is the sum of the area of all armour wires, l_a the length of the wire per rotation around the cable, β the angle between l_a and cable radius, and γ the angular time delay of flux density B with respect to the magnetising field H . The real term in the equation above comes from the longitudinal permeability μ_e being a complex number where $\mu_e = |\mu_e|[\cos(\gamma) - i \sin(\gamma)]$. For a more thorough explanation of the terms in Eq. (3.20) the reader is referred to article [13].

If the armour and sheath is non-magnetic ($\mu_r \approx 1$) the current in the sheath-armour in cable k is

$$I_{sa_k} = -\frac{I_{c_k} * i\omega L_k}{R_e + i\omega L_k} \quad (3.21)$$

Adding this to the current in the conductor gives to effective current of the given cable. The effective current can the be used when calculating the magnetic field peak in Eq. (3.6). Note that Eq. (3.7) is not valid as the effective currents of the cables isn't necessarily 120° phase shifted to each other. As the induced current is, to some extent, out of phase with the conductor's the effective current of the cable is lower than the one in the conductor, making the magnetic field lower as well.

3.1.3 Effect of seawater

The following derivation is a modified version of the derivation by David Meeker [20]. Said derivation is for a radially finite steel pipe with a single conductor in it. In this thesis this has

been extended to a three-phase power system in the sea.

Alternating magnetic field induces a current (eddy currents) in seawater. This affects the magnetic field by reducing its magnitude and phase. Effectively, it can be seen as the ocean has a magnetic impedance.

From the work of Stoll [30] the magnetising field H [A/m] around a circular cylinder is

$$\frac{d^2H}{dr^2} + \frac{dH}{dr} - (\alpha + \frac{1}{r^2})H = 0 \quad (3.22)$$

Where $\alpha = (1 + i)/\delta$ is a propagation constant and $\delta = \sqrt{\frac{2}{\omega\sigma\mu}}$ is the skin depth of the material. The skin depth relates the decay of an alternating current toward the centre of a material.³.

The solution for H is

$$H = c_0 M(\alpha r) + c_1 N(\alpha r) \quad (3.23)$$

Where M and N are first order modified Bessel functions of the first and second kind respectively.

The boundary conditions can be found from Ampere's loop law as

$$\oint H dl = \iint J dA \quad (3.24)$$

Where J is the current density in the wire.

Now from Ampere's/Biot-Savart law, the inner boundary is

$$H_{inner} = \frac{I}{2 * \pi * r_i} \quad (3.25)$$

Where the inner radius is the surface of the cable, I is the complex valued current in the conductor and armour/sheath.

In [20] the outer boundary is the outside of the steel tube. And as the tube isn't infinite in longitude length the same current has to flow back the tube as in the wire giving a net current of the entire cylinder of $I_{net} = 0$. The cable in this case is also finite, but the ocean has no clear outer boundary. However, the skin depth δ_{ocean} at 50Hz is about 30m. So it can be assumed

³Alternating currents tends to have higher current density at the surface than at the centre of the conductor

that the eddy currents are fully attenuated after $10 * \delta_w = 300m$ with an *error* $< 0.005\%$ [28]. Effectively, this assumption states that no currents are induced from the cable at a 300m radial distance, making the net current $I_{net} = 0$ over a cylinder of saltwater with $r = 300m$. The outer boundary condition becomes.

$$H_{outer} = \frac{I}{2 * \pi r_o} \quad (3.26)$$

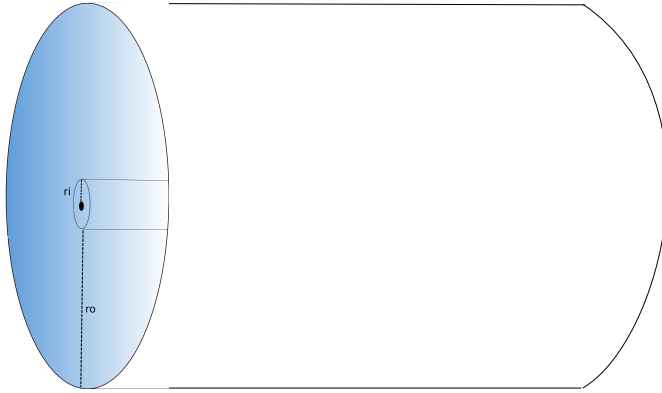


Figure 3.1: Wire,cable and enclosing cylinder of 300meter seawater.

With these boundary conditions it is possible to solve for c_0 and c_1

$$c_0 = \frac{I}{2\pi} \left(\frac{r_i N(\alpha r_i) - r_o N(\alpha r_o)}{r_i r_o (M(\alpha r_i) N(\alpha r_i) - M(\alpha r_i) N(\alpha r_o))} \right) \quad (3.27)$$

(3.28)

$$c_1 = \frac{I}{2\pi} \left(\frac{-r_i M(\alpha r_i) + r_o M(\alpha r_o)}{r_i r_o (M(\alpha r_i) N(\alpha r_i) - M(\alpha r_i) N(\alpha r_o))} \right) \quad (3.29)$$

Using c_0 and c_1 in Eq (3.23) gives the magnetic field at any radius r .

The magnetic field flux density B from cable k is

$$B_k(r) = \mu_0 \mu_r H(r) \quad (3.30)$$

And

$$B_{k_{xy}}(r) = B(r) * (z_l - z)/r \quad (3.31)$$

$$B_{k_z}(r) = B(r) * (((xy)_l - (xy))/r \quad (3.32)$$

Note that $B_k(r)$ is complex valued and the magnitude and phase changes with r .

For multiple cables the r for a given cable is given by

$$r = \sqrt{(x - x_l)^2 + (y - y_l)^2} \quad (3.33)$$

Where x_l and y_l is the location of the cable. The peak field is again found by the complex absolute value as shown in the first section.

$$B_{tot_z} = \sqrt{|B_{1_z}(r) \cdots + B_{n_z}|^2} \quad (3.34)$$

$$B_{tot_{xy}} = \sqrt{|B_{1_{xy}}(r) \cdots + B_{n_{xy}}|^2} \quad (3.35)$$

$$(3.36)$$

The total field is obtained by using the sum of the conductor current and shield-armour current (Eq. 3.21) in the inner and outer boundary conditions (Eq. (3.25) and (3.26))

3.1.4 Effect of burial

The soil will affect the magnetic field in much the same way as the seawater. However, the seawater is usually the dominating medium between the AUV and the cable. This follows from the REMUS 100 AUV flying at least 3m over the ground and that the cables rarely are buried that deep[3]. Further, the conductivity of the soil will generally be much lower than that of seawater[4]. Depending on its conductance it can therefore be accounted for in two ways. If the conductance is very low, it can be assumed to non-conductive, this is achieved by increasing the radius of the inner boundary in Eq. (3.25). Naturally, this requires an initial guess of the buried depth. Another method is to approximate the soil as seawater. This is fair when the conductivity is not that much smaller or/and when the buried depth is small compared to the overall distance between the AUV and cable. In [28] the conductivity of

the soil is approximated from the conductivity and density of the soil-material, and that of seawater. In this thesis, it's assumed that the buried depth is small compared to the overall distance between the AUV and cable and the soil is approximated as seawater.

3.2 Cable Localisation

This section presents techniques to locate AC cables from the magnetic field they produce. First, a method is derived for locating a single phase AC cable. This method is then further augmented to locate three AC cables in a three-phase system. Lastly, a new method is derived for the tracking and localisation of three cables in a three-phase system. In all these derivations it's assumed that the magnetic field amplitude from the cable has been perfectly isolated and is noiseless. Methods attempting to achieve this is explained in the next section.

3.2.1 Single phase AC Cable

This location method is derived in an article by Xiang. Yu [36], and is probably the underlying equations used for both Orion and SmartTrack, but this is unconfirmed. In this thesis the derivation is modified so both magnetometers are on one side of the cable. This differs from [36] where the magnetometers are on each side of the cable. The magnetometers are here on the same side to account for Remus 100 AUV not having wings and thus greatly limiting the magnetometer spacing.

An illustration of the AUV over a single phase AC cable is shown in figure 3.2

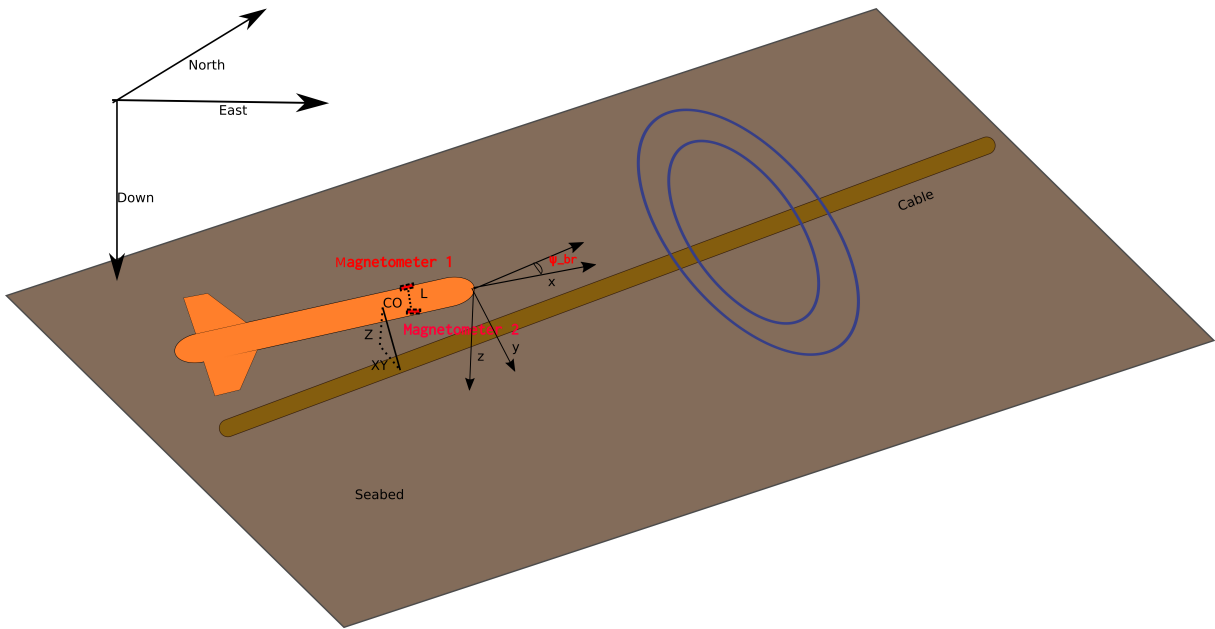


Figure 3.2: The AUV and cable as they are located in the derivations of this method. The origin of the BODY-frame is actually in CO, but drawn at the bow to make the drawing less clustered.

The notations are as follows: L is the distance between the magnetometers, CO is the origin of the BODY-frame, $[x, y, z]$ are the body frame axes, XY is the BODY-frame "horizontal" distance and Z is the BODY-frame "vertical". Both are in the BODY-frame meaning that the "vertical" and "horizontal" distance is depended on the pitch and roll.

Relative Heading

The axes of the magnetic field will vary with the heading of the AUV relative to the cable

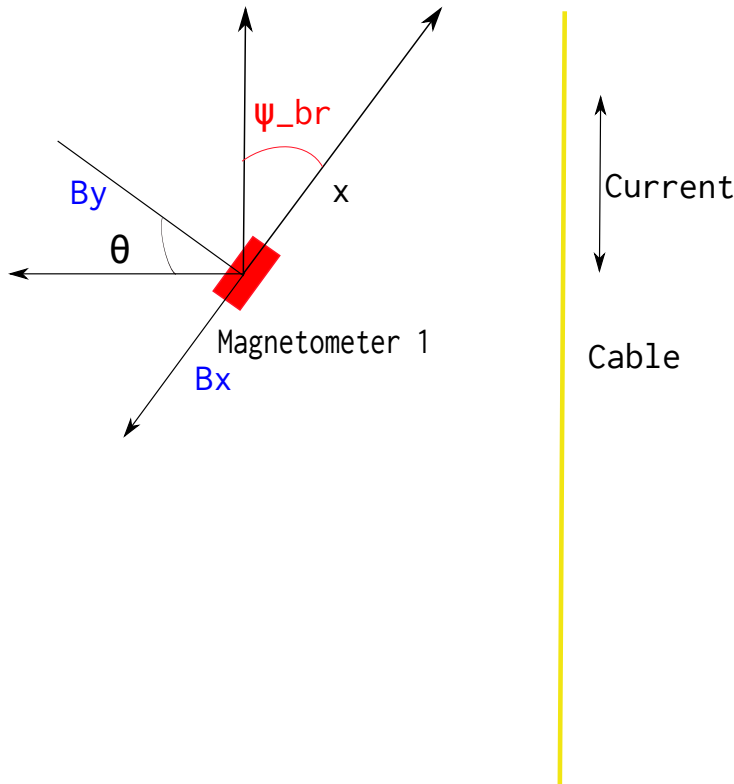


Figure 3.3: AUV and cable as seen from above, the relative heading is the angle between B_x and B_y .

Figure 3.3 shows an illustration of an AUV with one magnetometer and a cable. The magnetic field recorded by the magnetometer is given in the BODY frame. From Figure 3.3 it is seen that $\theta = \psi_{br}$. From this the relative heading can be calculated by

$$\psi_{br} = \arctan\left(\frac{B_x}{B_y}\right) \quad (3.37)$$

If the heading of the AUV is known the NED heading of the cable is given as

$$\psi_c = \psi_{br} - \psi_{AUV} \quad (3.38)$$

As an effect of the FFT both B_x and B_y will be positive. Therefore the relative heading will always be in the first quadrant. To compensate for the lack of sign the phase shift can be used. If B_x and B_y are in-phase both are positive. If B_x and B_y are 180 degrees phase-shifted then one is negative. It is of no importance which is negative as the AC induced magnetic field constantly changes direction and that, technically, a cable heads both ways. B_x and B_y are in phase if the cable is heading in the first and third quadrant and out of phase if it's

heading in the second or fourth quadrant.

Localisation

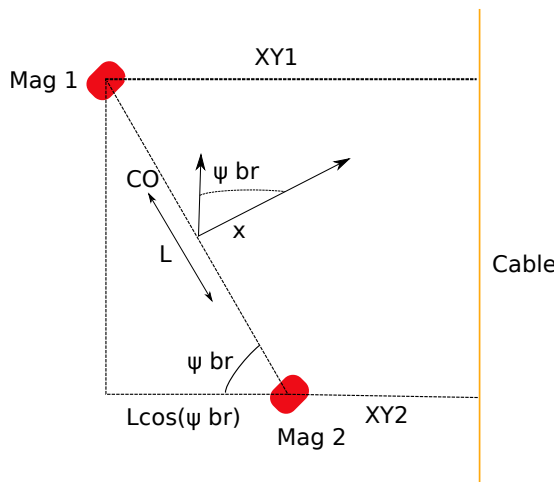


Figure 3.4: AUV and cable from above

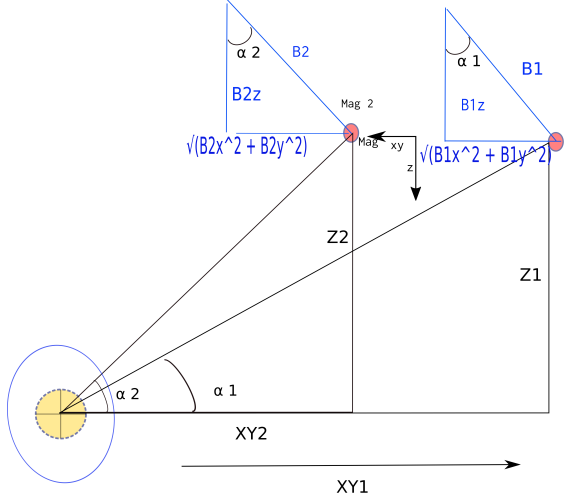


Figure 3.5: AUV and cable from the front

The similar triangles in figure 3.5 leads to the following expressions.

$$\tan(\alpha_1) = \frac{\sqrt{B_{x1}^2 + B_{1y}^2}}{B_{1z}} = \frac{Z_1}{(XY)_1} \quad (3.39)$$

$$\tan(\alpha_2) = \frac{\sqrt{B_{x2}^2 + B_{2y}^2}}{B_{2z}} = \frac{Z_2}{(XY)_2} \quad (3.40)$$

From figure 3.4 the relationship between the horizontal distances $(XY)_1$ and $(XY)_2$ is

$$(XY)_1 = (XY)_2 + L_1 \cos(\psi_r) \quad (3.41)$$

Where L_1 is the distance between the two magnetometers and ψ_r is the relative heading.

Inserting equation (3.39) and (3.40) in equation (3.41) gives

$$Z = \frac{B_{1y} \sqrt{B_{2x}^2 + B_{2y}^2}}{B_{1z} \sqrt{B_{2x}^2 + B_{2y}^2} - B_{2z} \sqrt{B_{1x}^2 + B_{1y}^2}} L_1 \quad (3.42)$$

where Z is the distance in the BODY-frame down.

For a known Z the horizontal distance is

$$(XY) = (XY)_1 + \frac{((XY)_2 - (XY)_1)}{2} \quad (3.43)$$

Where $(XY)_1$ and $(XY)_2$ are given by equation (3.39) and (3.40). Note that Eq. (3.42) is undefined if heading directly towards the cable because the two magnetometers gives equal measurement and a division by zero occurs. The BODY-frame distance can be transformed to the NED-frame by the rotation matrix (2.25), and the buried depth is found by subtracting the distance to the ground. On Remus 100 AUV the rotations needed for the rotation matrix and the buried depth can be found by payload sensors. Specifically, the magnetic compass, for heading; the gyroscope, for pitch and roll; and the ADCP, for the distance to ground. For the buried depth it's assumed that the cable, ground, and AUV have equal pitch.

As the FFT always gives positive values, Z and H will always have the same sign. It can be fairly assumed that the cable is below the AUV giving a positive Z . However, it's unknown whether the cable is a distance of H to the right or to the left. Fortunately, assuming that the cable is beneath the AUV makes it possible to use the phase shift between B_z and B_y to obtain the direction. As illustrated in Fig 3.6 where X is into the plane, B_z and B_y have the same sign if the cable is to the right of the AUV and opposite signs if the cable is to the left. As before, same sign will correspond to in-phase from the FFT and opposite signs correspond 180° phase shifted to each other.

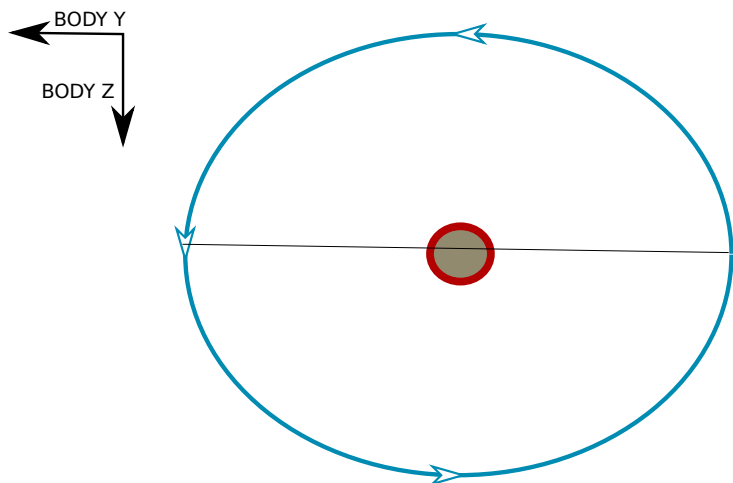


Figure 3.6: The direction of the magnetic field for BODY Z and Y Axis. When the cable is to the right of the AUV B_z and B_y has the same sign at all times, after Fourier transforming this corresponds to in-phase. The opposite is true on the other side.

Finding the direction by the phase also serves another purpose. The relative phase between them B_z and B_y is used it is far more resilient towards noise than when triangulating into the cable's exact position. This follows from the noise needing to be as big as the field to change the phase by over 90° , while only a small error will make an effect on Eq. (3.42). The phase shift can therefore be used to find the direction to the cable when it's too far away to pinpoint. This can, naturally, be used to guide the AUV closer.

3.2.2 Three-Phase Power System

In this section a method for tracking and locating the cables in a three-phase power system is derived. Two methods are used, but the first method is to assume that each cable can be approximated as a signal AC cable. This allows for using the triangulation method derived in the previous section. This method is not restated here. The next method is for when this approximation isn't valid and is divided into two parts. An online part that finds the direction to the cables for tracking, and an offline part which is used to pinpoint their location. The separation is mainly because it is unnecessary to know the exact position of the cables during the survey and fully implementing this would greatly increase the complexity of the online code.

Cable Tracking (online)

For the accurate offline cable localisation of three cables it is desired for the AUV to fly along the cables, but in a zigzag pattern where it crosses the outer cables before returning. This is to get many points of measurements for a LSQ-curve fit on the data.

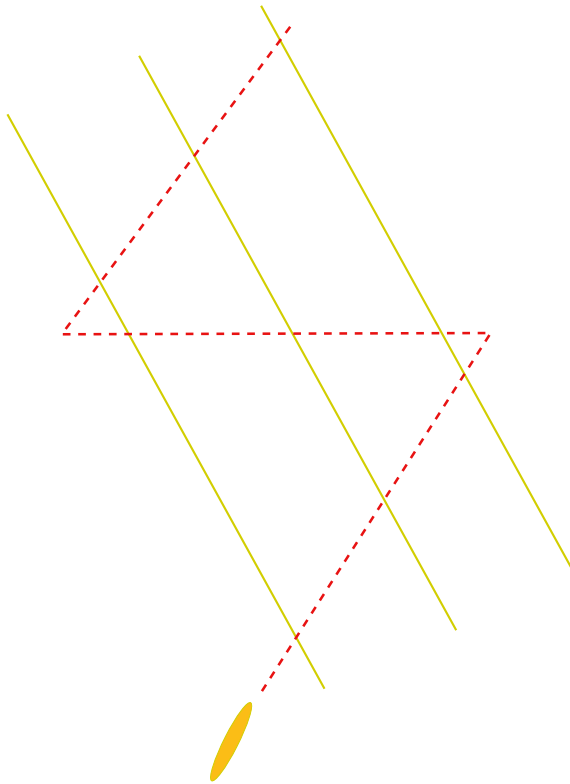


Figure 3.7: The AUV's desired path along the three cables.

Relative heading As for one cable it is still possible to determine the relative heading of the cables by

$$\psi_{br} = \arctan\left(\frac{B_x}{B_y}\right) \quad (3.44)$$

The assumptions for this to be valid is

- All cables are parallel
- The cables heading are solely in the XY-plane with respect to the AUV (equal pitch of cable and AUV).

When these assumptions are met the relation between B_x and B_y is not affected by the elliptical polarisation of the three-phase field.

Left, right or in-between To zigzag across the cables it's necessary to know whether we are left, right or in-between the cables. As for a single phase AC cable the phase shift between B_{xy} and B_z will change to the sides of the cables. However, the accurate mathematical description is far more complex. Nevertheless, when the outer cable is dominating the same

phase shift applies. Dominating means that the peaks of this cable are at the same time as the peaks for the total field. As a rule of thumb this occurs when the AUV is at least as far outside the outer cable horizontally as it is vertically. As for one cable the phase between $(\angle B_y - \angle B_z) \rightarrow 0^\circ$ while when all the cables are to the left $t(\angle B_y - \angle B_z) \rightarrow 180^\circ$.

In-between the cables the phase shift is changing rapidly, and is close to 0° or 180° only when very close to a cable. A posterior probability function is therefore employed to state to which direction the AUV should move. Naturally, it should move from one direction, through the in-between phase, and only return when the opposite direction is given.

The residuals between left or right can be set to

$$e_1 = (180 - \text{abs}(\text{phase})) \quad (3.45)$$

$$e_2 = (0 - \text{phase}) \quad (3.46)$$

$$e_3 = (150 - \text{abs}(\text{phase})) \quad (3.47)$$

$$e_4 = (30 - \text{abs}(\text{phase})) \quad (3.48)$$

Where 1 and 2 corresponds to the cables left and right side respectively. 3 and 4 are residuals that corresponds to the field in-between the two outer cables.

The posterior probability function is a strict simplification of the Kalman filtering posterior probability evaluator (PPE) described in [27] and used in [11]. It is here greatly simplified by omitting of the error variance matrix and effectively becoming just a recursive probability function. The probability for a given situation is

$$P_i(t+1) = \frac{e^{w e_i^2}}{\sum_{j=1}^{j=4} P_j(t) B e^{e_j^2}} \cdot P_i(t) \quad (3.49)$$

Where w is a *forgetting factor* and is used to weight new measurements more than old. It is here tuned to achieve the desired aggressiveness of change. Also, a dwell time σ is used to prevent too fast switching.

Cable localisation (offline)

Least Squared Fit The data sampled when moving from one outer cable to the outer cable can be curve fitted to the mathematical model derived earlier in this chapter. Either just Biot-Savarts law Eq (3.7), or the full mathematical model including the effect of sheath-armour and seawater. The tuning parameters in the curve fit model is then the locations of the cables'. This is carried out offline as it computational inefficient and even online the cable would still be found after the AUV has passed over them. Here, the data is curve fitted by the least-squared-curve fit algorithm. The function being minimised is given in Eq. (2.32).

3.3 Signal processing

In this section required procedures to acquire usable measurements are presented. This includes isolating the cables generated field, calibrating for ferromagnetic disturbances and compensating for misaligned axes between the AUV and magnetometer.

3.3.1 Isolating the cable-generated field

The cable-generated magnetic field is isolated from fields of other frequencies by the FFT. To estimate the amplitude of the signal it must be sampled for at least one period. As one period is $\frac{1}{50}$ of a second it is assumed that the AUVs' position and attitude are constant during this time. Sampling for a longer time will average white noise, but a long sampling time negates the assumption of constant attitude and position.

For Sampling rates above the Nyquist frequency (100Hz) the cable's signal is recorded as a 50Hz signal and the index corresponding to the cable is given by Eq. (2.29). For a lower sampling rate, equation the corresponding aliased frequency must be used [14].

3.3.2 Calibration

The calibration on the magnetometers should account for three different sources of error. The misalignment of the magnetometer axes to the BODY-frame, a static magnetic field from

ferromagnetic objects, and a static field induced by the DC current on board.

Ferromagnetic distortion

Ferromagnetic disturbances can be divided into a hard-iron and a soft-iron distortion. The Hard-iron effect is a magnetic field produced by a ferromagnetic material in close vicinity and gives a constant offset. The soft-iron effect comes from materials that does not necessarily produce a magnetic field, but skews other magnetic fields toward itself, such as the earth's and a cable's. For AC cable localisation only the soft iron is an issue as the hard iron is filtered ut by the Fourier transform. Nonetheless, a routine to calibrate for both is presented here.

When plotting the magnetic field axes with respect to each other. The hard-iron offset causes a nonzero origin while the soft-iron skews the plot to be spherical instead of cylindrical. An illustration is shown in Figure 3.8.

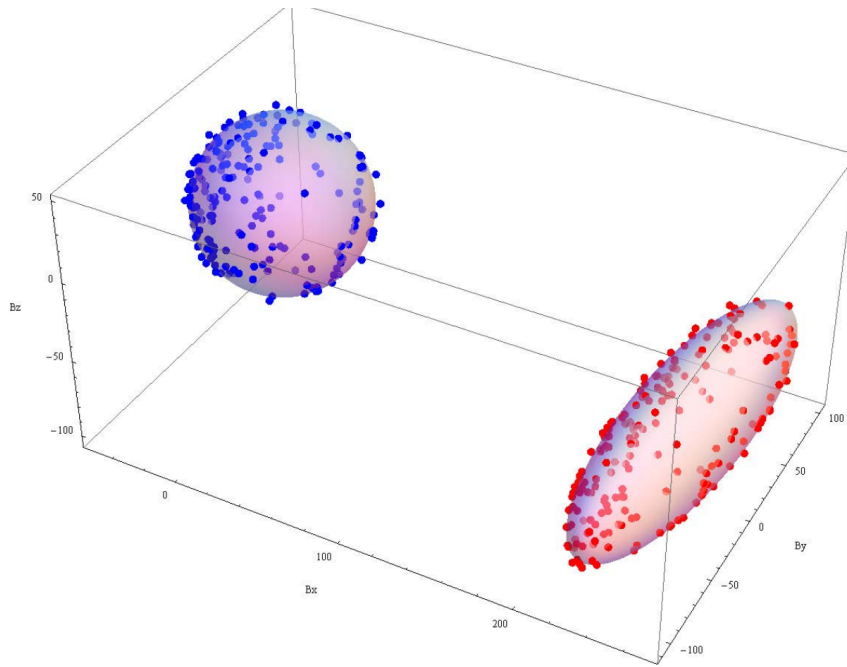


Figure 3.8: The blue dots are from a calibrated magnetometer while the red are from an uncalibrated. The position offset visualises the hard iron offset, while the spherical form of the red dots shows the effect of soft iron. Figure from [8]

Remus 100 AUV is very limited in pitch and is not actuated in roll. Thus, the calibration routine only accounts for yaw rotation. The 3d sphere in Figure 3.8 then becomes a 2d circle.

The AUV is rotated in circles in yaw and the peak values $B_{x,y_{max}}, B_{x,y_{min}}$ are stored for both the X and Y axis.

Hard-iron calibration is achieved by adding to each component the sum of

$$B_{x,y} = B_{x,y} + \frac{B_{x,y_{max}} + B_{x,y_{min}}}{2} \quad (3.50)$$

Effectively, this moves the origin to [0, 0]

For an optimised soft-iron correction a transformation matrix should be used. Here an averaging algorithm is used, equal to a diagonal transformation matrix.

The principle axes of the ellipsoid are

$$r_x = \frac{B_{x_{max}} - B_{x_{min}}}{2} \quad (3.51)$$

$$r_y = \frac{B_{y_{max}} - B_{y_{min}}}{2} \quad (3.52)$$

Taking the average of the axes the elliptical data can be scaled to a circular one by

$$B_x = B_x * r_{avg} / r_x \quad (3.53)$$

$$B_y = B_y * r_{avg} / r_y \quad (3.54)$$

Magnetometer misalignment

The magnetometer will not necessarily be mounted to perfectly align with the BODY-axes of the AUV. For a magnetometer with accelerometer it can easily be aligned by ensuring only acceleration in the z direction. Without accelerometer the magnetometer alignment is more complex.

The main issue is that the soft- and hard-iron affects the readings much like a sensor misalignment. Note that this correction must be carried out before the ferromagnetic calibration. It is presented after as soft- and hard-iron distortions should now be familiar concepts.

The follow assumptions are assumed to be valid

1. All hard- and soft-iron contributions are inside or attached to the AUV.
2. The magnetometer x-axis is perfectly aligned with x-axis of the AUV BODY-frame

The assumptions are fairly safe. The first is ensured by deciding the calibration location, usually at the sea surface. Given deep waters the main concern is the operators boat and it's no trouble moving this. The second assumption is fulfilled because the magnetometer casing used on REMUS 100 AUV is mounted directly along its axis with steel bars aligned with the AUV. This ensures equal pitch q and heading ψ . Only a roll angle p now remains. A misaligned roll angle between the AUV and the magnetometers occurs when the magnetometer is fitted into its casing. As the magnetometer is cylindrical it will fit for any rotations about its x-axis. The magnetometer is inserted by hand it's near impossible to make the alignment perfect.

By rotating the compass in yaw the max,min of $B_{y_{mag}}$ and $B_{z_{mag}}$ is found. The max and min of both is when the magnetometer's Y-axis is pointing north and south, respectively. Effectively, this removes the heading ψ from the equation and the rotation matrix for the x axis [32] gives

$$\max(B_{z_{mag}}) = B_{z_{earth}} \cos(p) SI_z + HI_z + B_y \sin(p) SI_y + HI_y \quad (3.55)$$

$$\min(B_{z_{mag}}) = B_{z_{earth}} \cos(p) SI_z + HI_z - B_y \sin(p) SI_y + HI_y \quad (3.56)$$

$$\max(B_{y_{mag}}) = -B_{z_{earth}} \sin(p) SI_z + HI_z + B_y \cos(p) SI_y + HI_y \quad (3.57)$$

$$\min(B_{z_{mag}}) = -B_{z_{earth}} \sin(p) SI_z + HI_z - B_y \cos(p) SI_y + HI_y \quad (3.58)$$

Where SI and HI are soft- and hard iron distortions respectively.

The difference between max and min values are

$$\delta_z = B_y \sin(p) SI_y \quad (3.59)$$

$$\delta_y = B_y \cos(p) SI_y \quad (3.60)$$

Finally the roll angle p is found by

$$\tan(p) = \frac{\delta_z}{\delta_y} \quad (3.61)$$

Inserting p , $\psi = 0$ and $q = 0$ in the rotation matrix (2.25) the magnetometer is aligned to the BODY-frame. This rotation should not be confused with the rotation to the NED-frame of the calculated positions of the cable; i.e. this rotation rotates the magnetometer readings to the BODY-frame, later the BODY-relative cable position is rotated to the NED-frame.

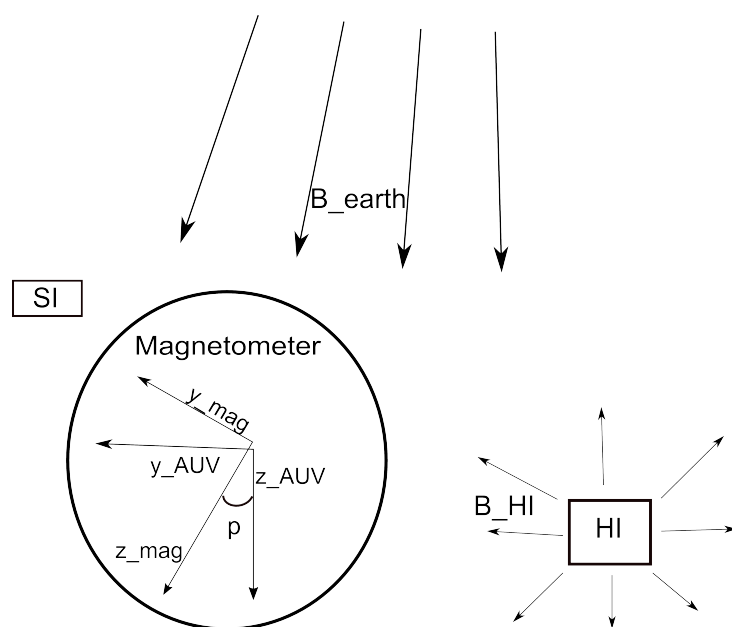


Figure 3.9: The magnetometer with a roll angle and in the presence of hard iron and soft iron disturbances. The hard-iron makes its own magnetic field while the soft-iron skews the earth's toward itself. North is into the paper

Chapter 4

Finite Element Analysis

In this chapter, the methods for describing the magnetic field and locating cables are tested on a simulated magnetic field obtained from Finite Element Analysis (FEA). The chapter starts by an overview of the created Finite Element Model. After this, results from simulations are presented. First comparisons are given between the magnetic field from FEA and the derived analytic model. Thereafter, results are shown for all the cable localisation methods.

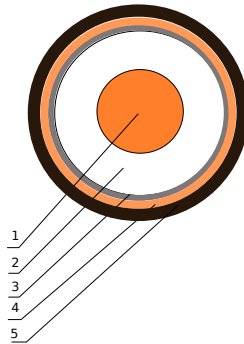
4.1 Modelling

To confirm the validity of the FEM models a model was created that is identical to the FEM model presented in an article for the Oregon Wave Energy Trust [28]. The latter was shown to concur with measurements from a similar real life case. The model compared against is a single phase AC cable. Both in the article, and in this thesis, a three-phase power system is simulated by superposition of this single AC cable. It's therefore deemed sufficient to confirm the model against only this single phase AC cable.

The identical model made in this thesis had near to equal result to the results in [28] thus implying correct modelling. The comparison can be seen in appendix A.

After the confirmation of correct modelling two cases were modelled. The cable model is a more or less accurate description of the TKZA 420kV cable used in Nyhamna. It differs in that the F3 lead alloy sheath is replaced by pure lead, and that all non-metal components are

replaced by acrylic plastic. Further, both the conductor and the armour are approximated as solids¹. No restrictions were set on the sheaths and armour which will let currents flow freely corresponding to a solid bonding.[6]. This is also the bonding used on the cables at Nyhamna [3]. An illustration of the cable is seen in Figure 4.1.



Element	Description	Thickness
1. Conductor	Solid Copper wire.	43.7mm
2. Insulator	Acrylic plastic	28mm
3. Lead Sheath	Mechanical pressure	3.6mm
4. armour	Flat copper wires	7mm
5. Insulator outer	Acrylic Plastic	20mm

Figure 4.1: Single Phase AC cable

For models to validate the mathematical models of the magnetic field the cable is assumed buried 1m beneath the soil. The parameters for soil and seawater are the same as used in [28] and given in figure 4.2



Figure 4.2: AC cable buried in the soil beneath the seabed

This cable was used in two different scenarios.

1. A single phase AC cable
2. Three AC cables in a three-phase power system spaced 9m apart

The latter should represent the scenario in Nyhamna. For validating the mathematical models of the magnetic field exact spacing of 9 meters are used. For cable localisation the distances are slightly tweaked in all axes to make the field less uniform and more accurately simulate real life conditions.

¹In reality they consist of many small wires

4.2 Finite Element Analysis Results

All the plots show the magnetic flux density B as function of horizontal distance. The vertical distance is constantly 4m for all plots. This representation is chosen instead of B as function of radial distance as it more accurately visualises the field when flying over the cables with an AUV.

4.2.1 Magnetic Fields

This section shows comparisons of the magnetic field from the mathematical models and the Finite Element Analysis.

Single Phase AC Cable

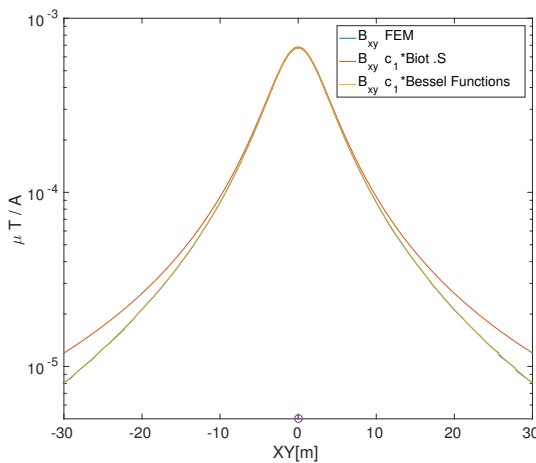


Figure 4.3: Horizontal component B_{xy}

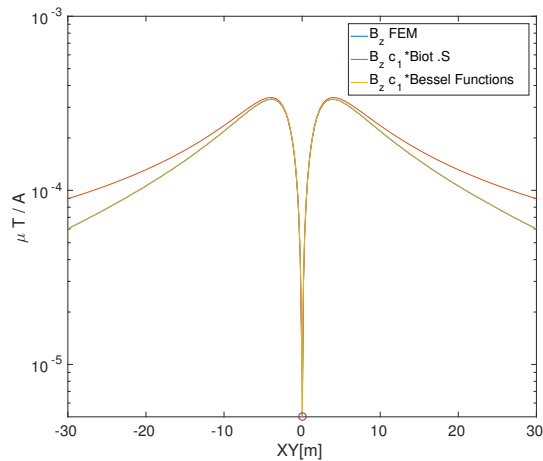


Figure 4.4: Vertical component B_z

Figure 4.5: Magnetic field from FEA and the analytic functions as a function of horizontal direction to the cable. The cable is located at [0, 0] and the AUV is flying over it with a constant vertical offset of 4m. The Bessel functions includes the effect of seawater while Biot-Savart law does not. c_1 is a tuned constant to compensate for sheath and armour. The FEM solution is almost identical to the Bessel functions and is therefore difficult to see.

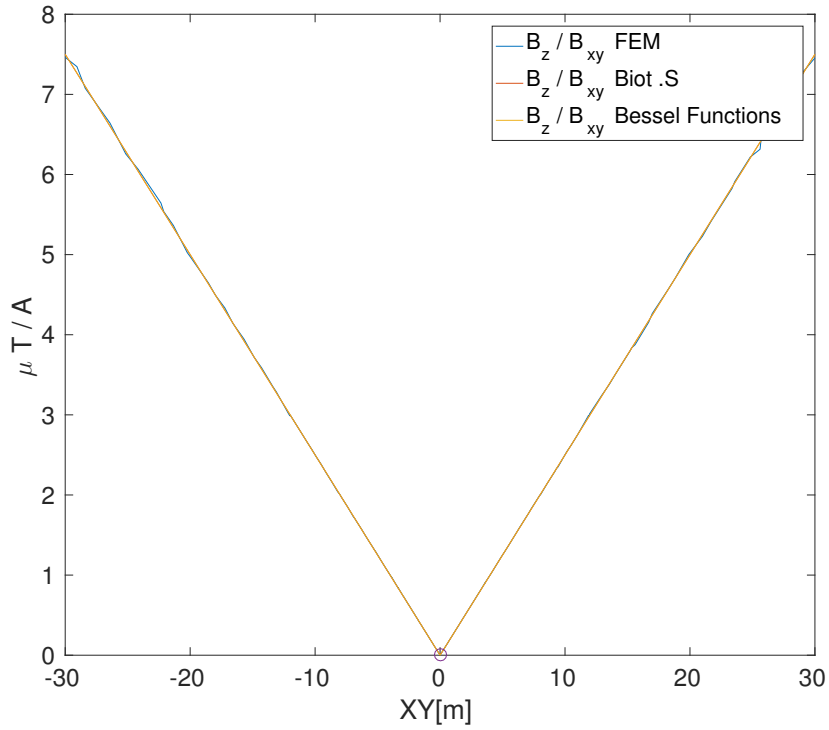


Figure 4.6: Relative strength between B_z and B_{xy} for FEM and analytic models. The cable is located at [0, 0] and the AUV is flying over it with a constant vertical offset of 4m.

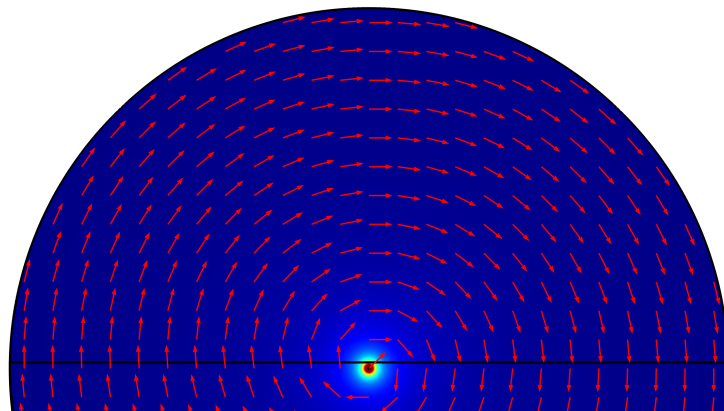


Figure 4.7: The direction of the peak magnetic field around a single AC cable from FEA. It is at all times perpendicular to the direction to the cable. The black line separates the soil from the seawater.

Figure 4.3 through Figure 4.7 shows plots of magnetic field around a single phase AC cable located in [0, 0]. In Figure 4.4 and 4.4 the Bessel functions (including the effect of seawater) concurs near-perfectly to the FEM-results when a constant $c_1 = 1/104$ is added to compensate for the sheath-armour. For Biot-Savart law in vacuum the field diverges at about 10m

distance from the cable.

In Figure 4.6 the relative strength between the components is equal for both models and FEM for all positions. The last Figure, (figure 4.7) shows the direction of the magnetic field is at all times perpendicular to the direction to the cable. Here the actual value is used stress this. From using the FFT on the magnetic readings the absolute value will be obtain, effectively making the arrows point in the same direction at both sides of the cable. This is the reason the phase shift is used to decide which side the cable is on as explained in section 3.2.

Three-Phase System

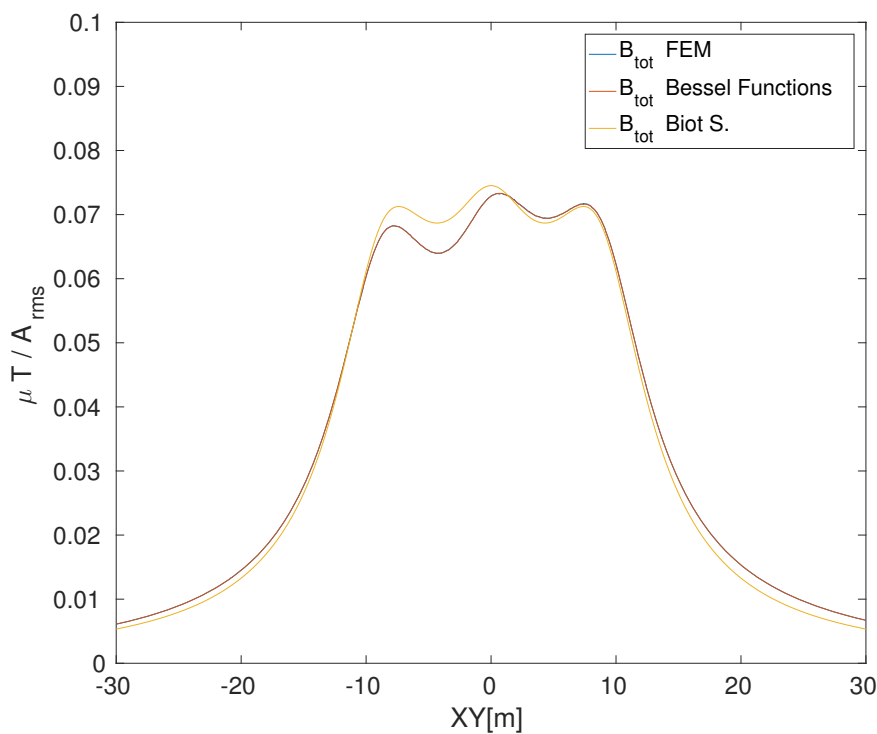


Figure 4.8: FEM and analytic magnetic flux density B_{tot} as a function of horizontal distance when hovering 4 meter above non-shielded cables in seawater. The cables are located in $XY_k = [-9, 0, 9]$. The total field as given by FEM and the Bessel functions are identical while the field from Biot-Savart law differs

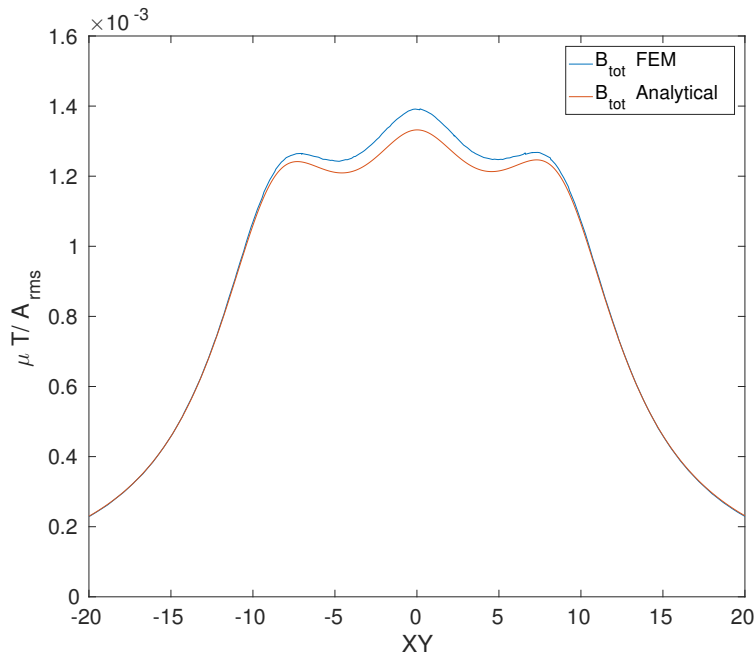


Figure 4.9: The magnetic flux density B_{tot} for both FEM and the analytic function including the effect of sheath-armour. B_{tot} is given as a function of the horizontal distance when hovering 4 meter over shielded cables in air. The cables are located in $XY_k = [-9, 0, 9]$. Note that the field is about 60 times lower than for unshielded cables

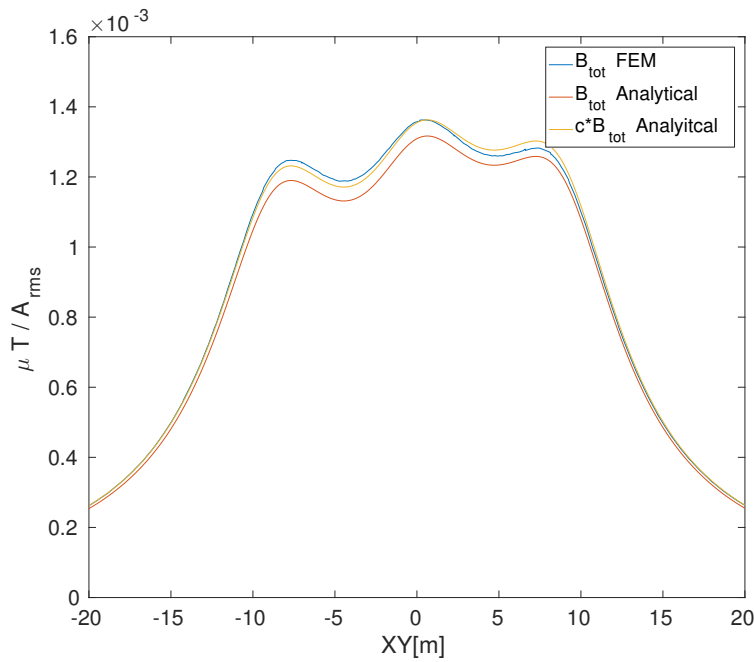


Figure 4.10: FEM and analytic magnetic flux density B_{tot} as a function of horizontal distance when hovering 4 meter above shielded cables in seawater. The cables are located in $XY_k = [-9, 0, 9]$.

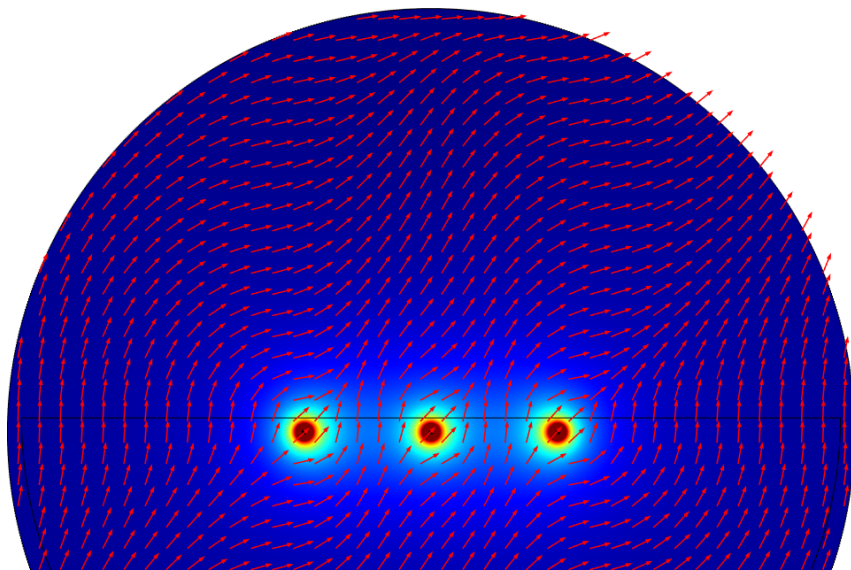


Figure 4.11: Direction of the magnetic field around a three-phase power system

Direction of the Magnetic field for three AC cables. The XY and Z components are absolute values. As it is absolute values the actual direction of the field will therefore not necessarily correspond to the arrows shown above. It will, however correspond to the field obtained by the FFT. Note that the field is not consistently perpendicular to the direction to the cables.

Figure 4.8 to figure 4.11 shows the magnetic field over a three-phase system for different scenarios. The first plot shows the magnetic field over non-shielded cables in seawater (figure 4.8). In this plot the FEM model and the Bessel functions have perfect concurrency. Biot-Savart law, however, does not take into account the effect of seawater and differs in the results. This is clearly seen by the symmetry of this graph about $XY = 0$. The perfect concurrency implies that approximating the soil as seawater was a valid assumption.

Figure 4.9 compares FEM with the effect of sheath-armour. Note that the magnetic field is about 60 times lower than for the non-shielded cables in figure 4.8. In spite of this the analytic model only has a slight discrepancy in that the field above the centre cable is understated. The largest difference (at the centre) is 7%.

When the two cases are combined in 4.10 the mathematical model only slightly understates the field. The yellow graph shows the same function multiplied by $c_1 = 1.034$ which gives a very close fit to the total field. The mathematical slightly differs to FEA by overstating the

rightmost peak and understating the leftmost.

The last plot (figure 4.11) shows the direction of the field around a three-phase cable. Note that the arrows are pointing in the same direction on both sides of the cable. This is because the absolute value is used. This does not necessarily correspond to the actual magnetic field at the location. It will, however, correspond to the amplitudes as obtained by the FFT on the magnetometer data. The field is not consistently perpendicular to the direction to the cables and they can therefore not be located by triangulation.

4.2.2 Cable Localisation

Results from cable localisation methods on FEA data is presented in this section. The AUV is assumed to fly at a constant height of 4 meter over the cables. Further, the AUV moves from a horizontal distance of -30 meter on one side of the centre cable and to 30 meter on the other side. The current in the cable(s) is(are) $I_{RMS} = 100[A]$. For some simulations noise was been added. If not anything else is stated the noise is based on the FLC3-70 fluxgate magnetometer data-sheet [29]. Here the noise is stated to be $0.5[nT_{RMS}]$. This is modelled as Gaussian white noise with a zero mean and standard deviation $\sigma = 0.5[nT]$. Except from noise, no other restrictions are set on the magnetometer. That is, the field cannot be to weak to be detected, but the measurements will be useless when the noise is large compared to the field strength.

Single Phase AC Cable

Results from test of the trigonometric method described in section 3.2.1 is presented here. The REMUS AUV has a limit of 40cm magnetometer spacing, but it's here simulated with a 1.5m spacing as well as 40cm.

Without Measurement Noise

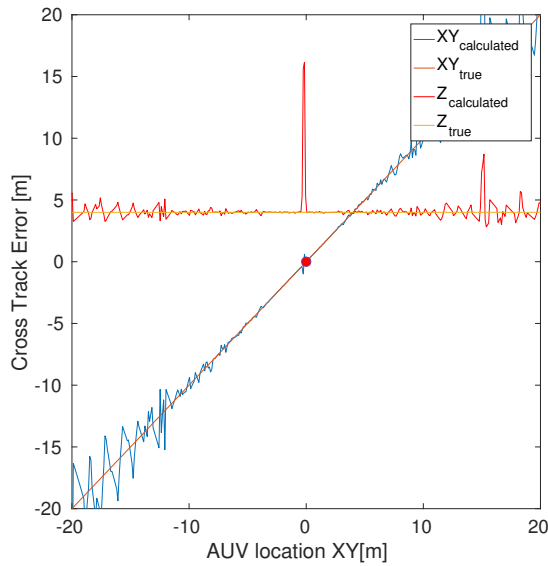


Figure 4.12: Cable localisation with 40cm Magnetometer spacing

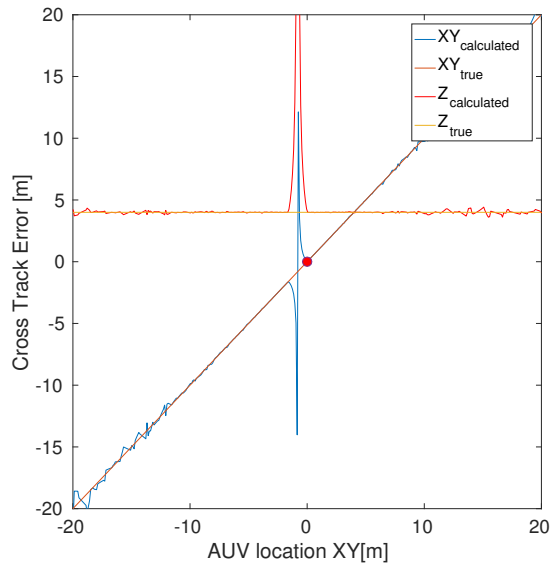


Figure 4.13: Cable localisation 1.5m magnetometer spacing

Figure 4.14: The figures shows the horizontal and vertical distances when the triangulation technique is applied to the magnetic field found by the single AC phase FEM model. The measurements are noiseless and the magnetometer spacing are 40cm and 1.5m. XY should concur with the x-axis of the plot, and Z should be constantly 4m. A true position is also shown.

With measurement Noise

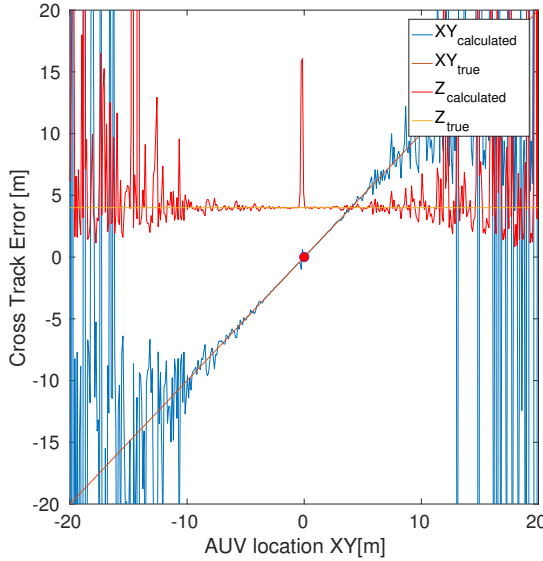


Figure 4.15: Cable localisation with 40cm Magnetometer spacing

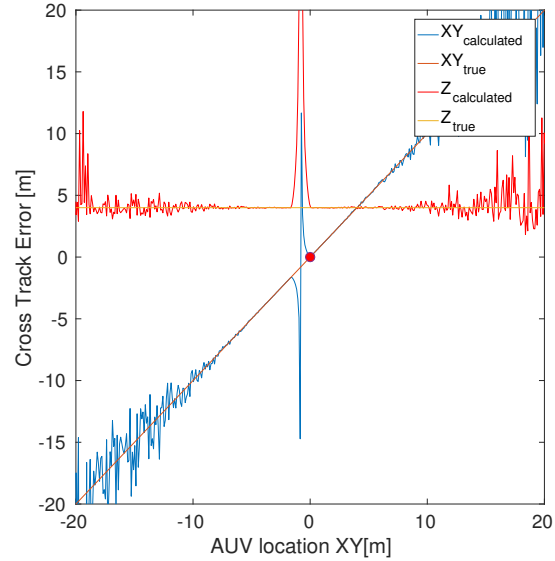


Figure 4.16: Cable localisation with 1.5m magnetometer spacing

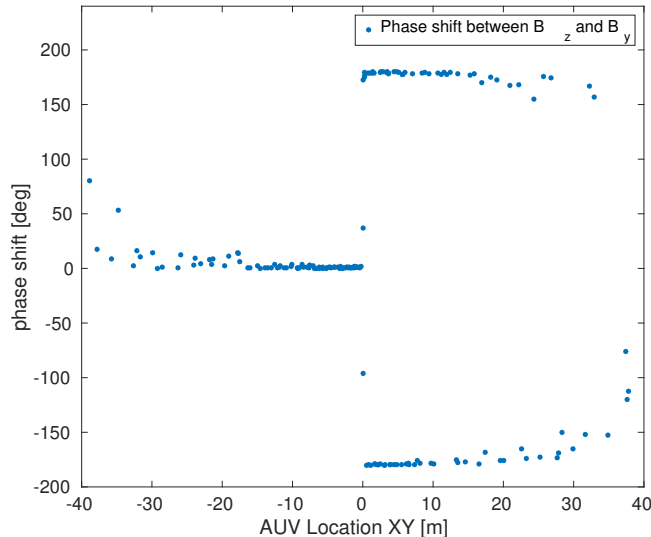


Figure 4.17: Phase shift between B_z and B_y for a single phase AC cable. Note that the x-axis is increased to 40m

Figure 4.18: Cable localisation when the AUV is crossing over a single phase AC cable with $I_{RMS} = 100[A]$. The AUV is hovering at a constant height 4m above the cable.

Figure 4.12 to figure 4.17 shows the results for cable localisation of a single AC cable. The triangulation method fairly calculates the correct position, even in the presence of measurement noise as seen in figure 4.15 and figure 4.16. It is apparent that the noise is suppressed when the the spacing of the magnetometers is increased. For 40cm spacing the cable is accu-

rately located at about 5meters horizontal distance while from 1.5m magnetometer spacing the localisation is very accurate for up to 10 meter horizontal distance. From the phase shift (figure 4.17) the correct direction to the cable can be found at up to 40[m] distance. The noise on the phase shift was simulated by adding the Gaussian white noise the real part of B_z and B_y before calculating the phase angle

$$\tan \phi_z = \frac{imag(B_z)}{real(B_z)} \quad (4.1)$$

For noiseless data as seen in figure 4.12 and figure 4.13 the calculated location is accurate to the end of the plot of 30m. It must be stressed that no restrictions, except noise, was put on the magnetometers. For noiseless data the the errors are therefore caused by numerical approximations in Comsol.

4.2.3 Three-Phase Power System

The results for localisation of cables in a three-phase power system are presented here. First, the cables are attempted to be located by assuming they are independent and using the triangulation method. After this, the curve-fitting method is used. The latter method is separated in two. First an online posterior probability function to decide the direction to the cables. After this, LSQ-curve fitting is performed on the FEM data. Both the full mathematical model and Biot-Savart law in vacuum are curve-fitted to the data and results are given for both.

Model

The model includes three cables located in $C_1 = [-8 - 1.5]$, $C_2 = [0 - 1]$, $C_3 = [9.5 - 0.5]$. The currents are $I_{left} = 100 * \sqrt{2}$, $I_{centre} = -70 - 122i$ and $I_{right} = -70 + 122i$. The cable layout is equal to the one for the single phase AC case and its specifications are given in figure 4.1. An illustration of the AUV with cables can be seen in figure 4.19.

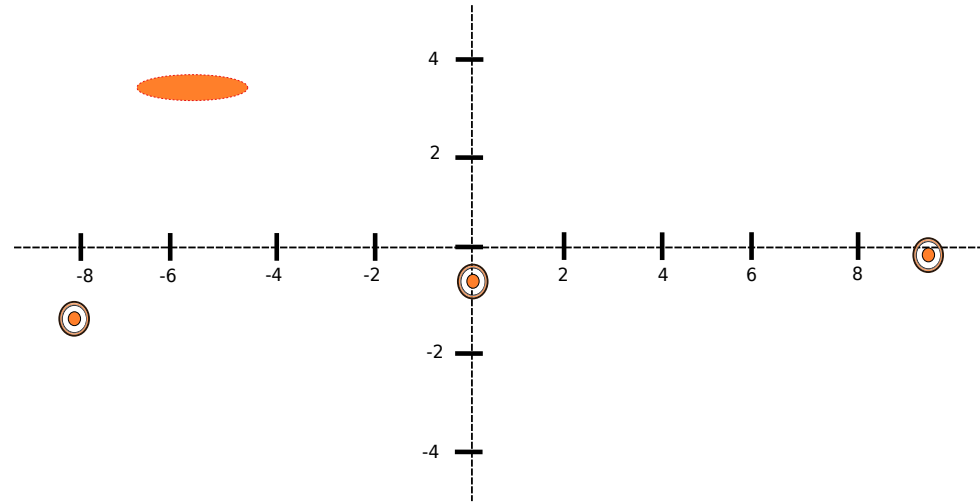


Figure 4.19: Illustration of the first FEM model

4.2.4 Single cable approximation

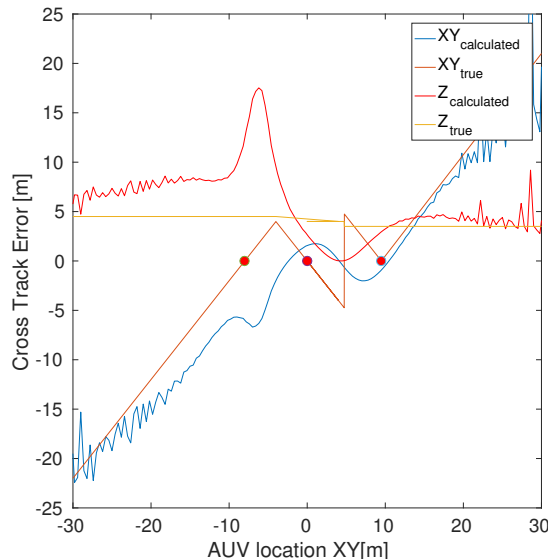


Figure 4.20: Single cable approximation without noise

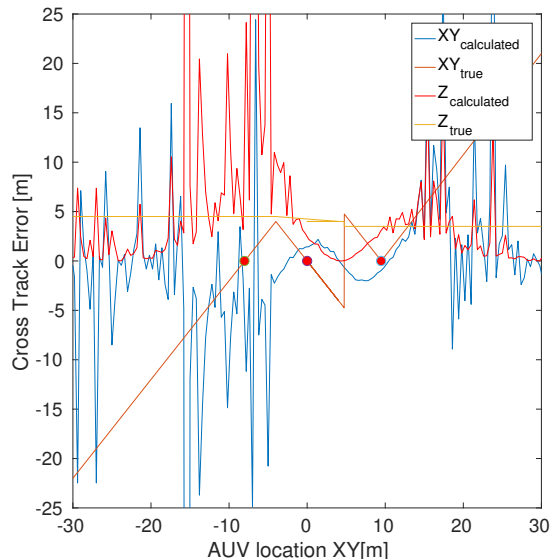


Figure 4.21: Single cable approximation with noise.

Figure 4.20 and figure 4.21 shows the position of the cables when approximating them as independent cables and triangulating. The yellow line shows the true vertical position and the orange the true cross track error. As can be seen in figure 4.20 the estimated positions are rather poor, but gives decent results on the far right end. When adding noise no consistency is present in the cable's estimated location. As before, the noise is Gaussian white noise with zero mean and a standard deviation of $\sigma = 0.5nT$.

4.2.5 Curve Fitting Method

Cable Tracking (online)

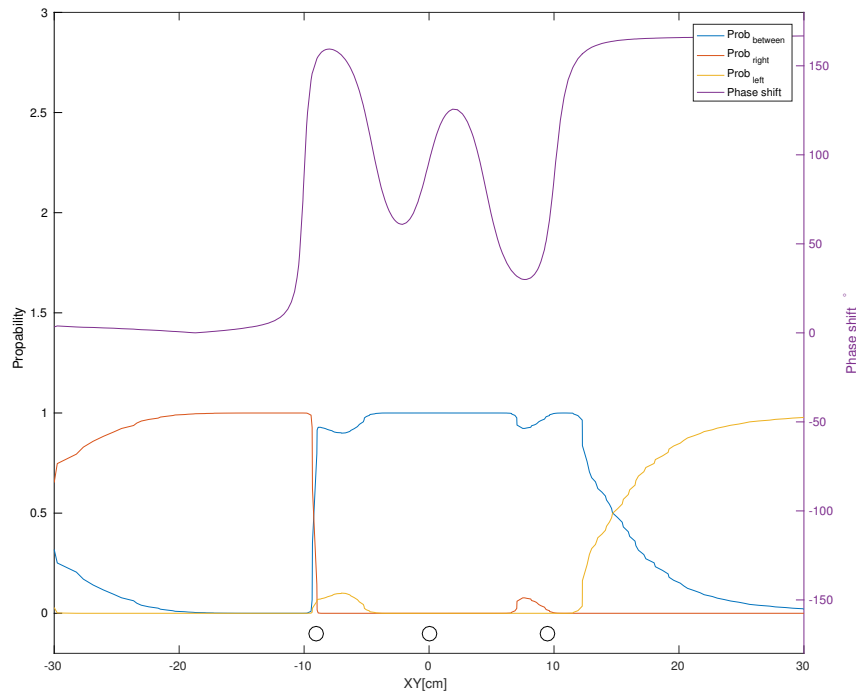


Figure 4.22: Online estimation of the direction to the cables'. The highest probability decides in which direction the cables are relative to the AUV. The purple graph responds to the right y-axis and is the phase shift between B_z and B_y . The other lines corresponds to the probability of a given direction and is with regard to the left y-axis. The circles at the bottom represent the locations of the cables.

Cable Localisation (offline)

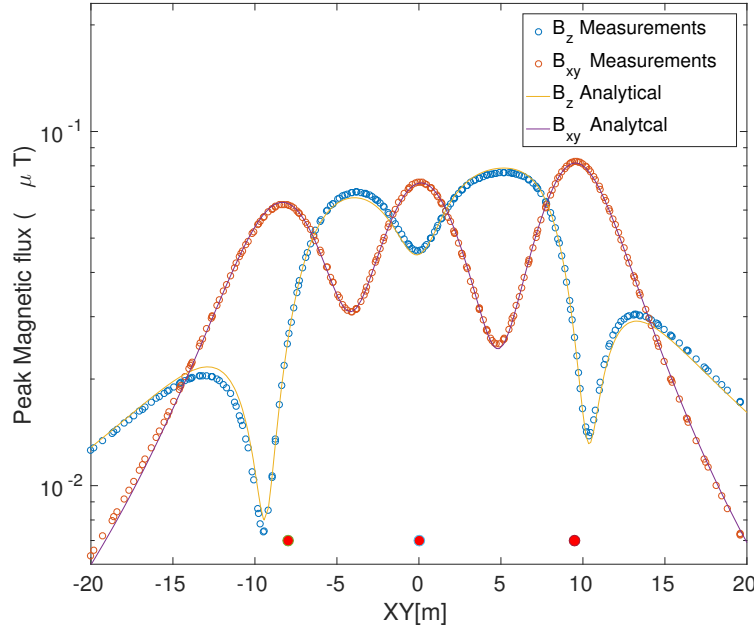


Figure 4.23: Curve fitting of the mathematical model of the magnetic field to FEM-data. The mathematical model used here includes both effect from seawater and armour-sheath. All the cables' positions as well as the current I in each cable are tuning parameters for the LSQ-curve fit Matlab solver. The circles at the bottom represents the locations of the cables.

Table 4.1: Estimated position of the three cables by least squared curve fitting to noiseless FEM data. Curve-fit model 1 represents the mathematical model derived including seawater and sheath-armour. Curve fit model 2 is the same mathematical model, but the current in the conductors are included as tuning parameters. The last column, is plain Biot-Savart law for three conductors in vacuum. Also with I_k as a tuning parameter.

Cable	Actual[m]	Curve-fit model1	Curve-fit model 2	Curve-fit model 3
C_{1xy}	-8	-7.62	-8.11	8.08
C_{1z}	-1.5	-3.6	-1.3	-1.26
C_{2xy}	0	0.4	0.12	0.10
C_{2z}	-1	-2.65	-1.06	-0.74
C_{3xy}	9.5	9.03	9.44	9.53
C_{3z}	-0.5	-2.6	-0.56	-0.35
I_{1RMS}	100	100	89.02	1.47
I_{2RMS}	100	100	91.4	1.54
I_{3RMS}	100	100	90.5	1.51
Total Position Error	0	7.0651[m]	0.6428[m]	0.8776[m]

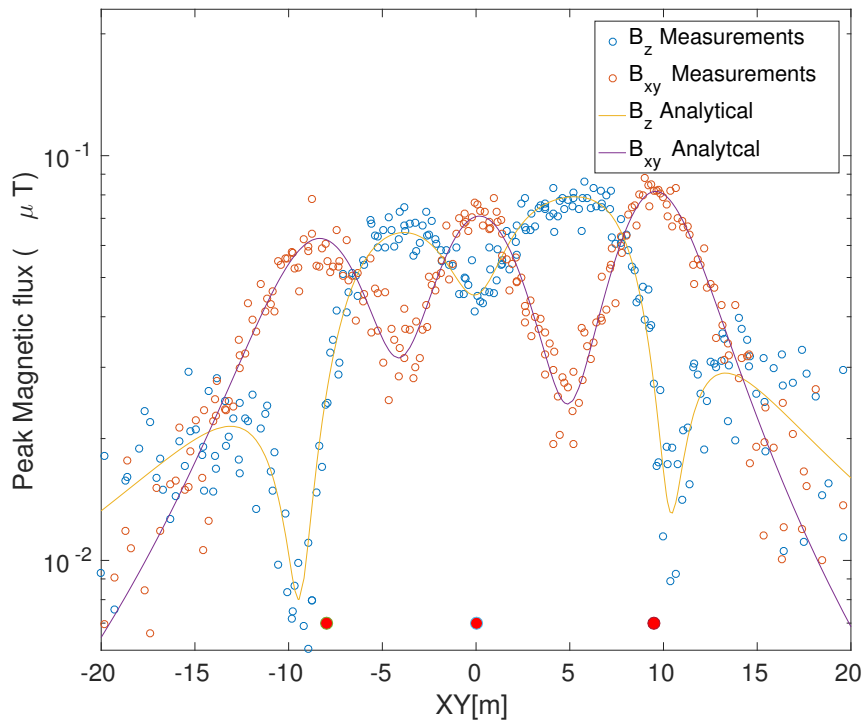


Figure 4.24: Curve fitting of the mathematical model of the magnetic field to noisy FEM-data. The mathematical model used here includes both effect from seawater and sheath-armour. All the cables' positions as well as the current I in each cable are tuning parameters for the LSQ-curve fit Matlab solver. The noise is Gaussian white noise with variance of $\sigma = 50\text{nT}$. Ten times the one in other simulations and the one given in the FlC3-70 datasheet

Table 4.2: Estimated position of the three cables by least squared curve fitting to noisy FEM data. Curve-fit model 2 represents the mathematical model derived in including the effect of seawater and sheath-armour. Curve-fit model 3 is plain Biot-Savart law for three conductors in vacuum. Both models has the cables's positions as well as their currents I as tuning parameters.

Cable	Actual[m]	Curve-fit model 2	Curve-fit model 3
$C_{1_{xy}}$	-8	-8.12	8.16
C_{1_z}	-1.5	-1.4	-1.34
$C_{2_{xy}}$	0	0.17	0.14
C_{2_z}	-1	-1.06	-0.76
$C_{3_{xy}}$	9.5	9.45	9.54
C_{3_z}	-0.5	-0.44	-0.23
$I_{1_{RMS}}$	100	91.47	1.47
$I_{2_{RMS}}$	100	92.36	1.55
$I_{3_{RMS}}$	100	91.28	1.1.51
Total Position Error	0	0.67[m]	1.072[m]

The last results, (figure 4.22 to table 4.2) are from cable localisation on a three-phase system. The results of the online code deciding the direction to the cables can be seen in 4.22. As can be seen the probability is greatest for the cables being to the right initially. As the AUV crosses the first cable this rapidly changes to a highest probability of the AUV being in-between cables. Lastly, when the AUV is crossing out the outer right cable the probability of the cables being left starts to grow and becomes greatest at about 15m. This is about 5.5 meters beyond the rightmost cable.

Curve-fitting are done with respect to three different mathematical models. Curve-fit model 1 represents the mathematical model that included seawater and sheath-armour. Curve-fit model 2 is the same mathematical model, but the current in the conductors are included as tuning parameters. Curve-fit model 3 is plain Biot-Savart law in vacuum, not accounting for either seawater or sheath-armour.

Curve fitting the derived mathematical model to data from FEA gives an almost perfect fit as seen in 4.24. The current and the positions are here the tuning parameters. Further, in table 4.1 the estimated locations of the cables are presented. When the curve-fit model assumes a fixed current the total position error is over 7[m]. Including the current as a tuning parameter

reduces this error down to $0.6[m]$. Allowing for tuning the current effectively compensates for unmodelled effects. Particularly, the imperfect modelling of the sheath-armour. This follows from the sheath-armour greatly reducing the overall magnitude of the field. For Biot-Savart Law the error is about $0.9[m]$, which is only 30cm more. Biot-Savart Law is not tested without allowing for a tuning of the current as the unmodelled sheath-armour will cause very erroneous locations.

The noise used for the curve fitting method was 10 times as high as for the triangulation method. This was because initial simulations showed near perfect results for the same noise levels. Nevertheless, for Biot-Savart law and the derived mathematical model the total position error from noisy data is $0.67[m]$ and $1.072[m]$. This is almost negligibly different from the noiseless results and slightly changes for each run as the generated noise differs. The curve-fit model not allowing for tuning of the current was not used here as the initial simulation of noiseless data (table 4.1) showed that this method was far worse than the other two.

Chapter 5

Experiments

In this chapter, the experiments that were carried out are presented. The same equipment is used for all cases. The experiments consist of testing both the cable localisation methods and the calibration routines. First the triangulation method is tested on single low-voltage AC conductor, before the curve-fit method is performed on a small-scale three-phase power system. After this, the field is measured at six single core cables buried in the same trench at Nidaros. The last cable test is on a Tere 1kv triplex cables which lays between Korsvika and Munholmen. This concludes the experiments on transmitting cables. The last two experiments are calibration of the magnetometer on the AUV. This includes both ferromagnetic calibration and compensation for misaligned sensors.

5.1 Equipment

A device was created to measure and process the magnetic field. The device consist of a Raspberry Pi-3(RPI) board-computer, a Labjack U6 digital to analogue converter (DAQ), a DCDC step down, and two FLC3-70 magnetometers. All components , except the magnetometers, were mounted on a board as seen in figure 5.1 and 5.2. A watertight housing was ordered to fit these components on REMUS 100 AUV. The magnetometers were put outside the AUV in water tight casings and connected to the device via watertight cables.

5.2 Code

All online code is written in C++ except the libraries that connects the RPI to the Labjack, which was written in C. For prepossessing, including least squared curve fitting and plotting, Matlab was used. The main code for cable localisation consisted of a C++ magnetometer class, a StreamData.c function for obtaining the magnetometer samples and a build in FFT function from the Armadillo C++ library. All other code is just an implementation of the equations derived for each method.

The main limiting factor for the equipment is the sample rate. Each magnetometer has 4 data cables, 3 for the magnetic field axes and 1 reference cable. For sampling a 50 Hz signal at least 100Hz sampling rate is needed, but 300Hz guarantees good readings. For two magnetometers and 8 data cables, which should all be sampled simultaneously, the sample rate per cable must be $8 * 300 = 2400\text{Hz}$.

By streaming data (letting the Labjack decide when to sample), the sample rate for close to 18bit resolution is 7200Hz. Meaning that all data is read at intervals of $1/900[\text{s}]$. Well beyond the requirement.

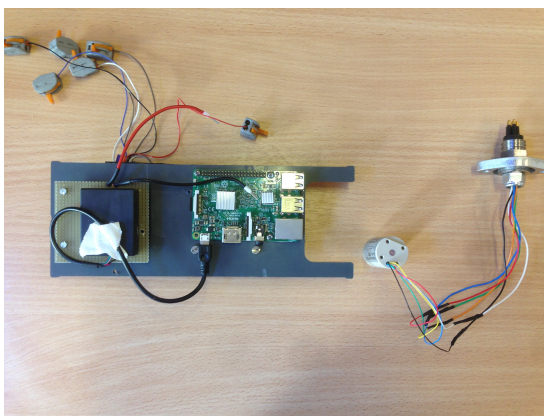


Figure 5.1: The device from one side seeing the DCDC converter on the left end of the board and the RPI on the other end

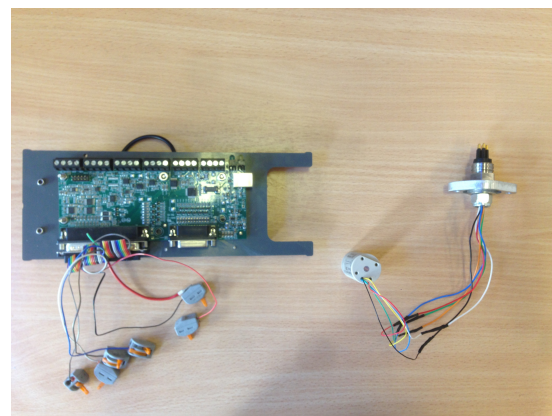


Figure 5.2: The other side of the board were the Labjack U6 is mounted. The magnetometer with the connector to the seacable is shown in the right side.

5.3 Marine cybernetics-laboratory

A low scale test was carried out for a single AC cable as well as for three-phase system. The conductors used were from a three-phase industrial fan heater. A figure of the device with three conductors is seen in figure 5.3

5.3.1 Single Phase AC Cable

One AC cable was put in the centre, while the two return currents were moved as far away as possible (about 50cm). The two magnetometers where then put with about 1cm spacing and the magnetic field were measured at 1cm regular interval from 0 to 20cm.

5.3.2 Three-Phase Power System

The cables were put 18cm apart as seen in Figure 5.3. The magnetometer was then moved from -60 to 60cm with sampling at 1cm interval's.

Unfortunately, the cables did not transmit equal current. By measuring the magnetic field at a fixed distance from each of them in turn the relative current was measured to be.

- Black = $1.2 * Gray$
- Brown = $0.5 * Gray$
- Gray = $1 * Gray$

This was used in the initial guesses for the LSQ-curve fit function.

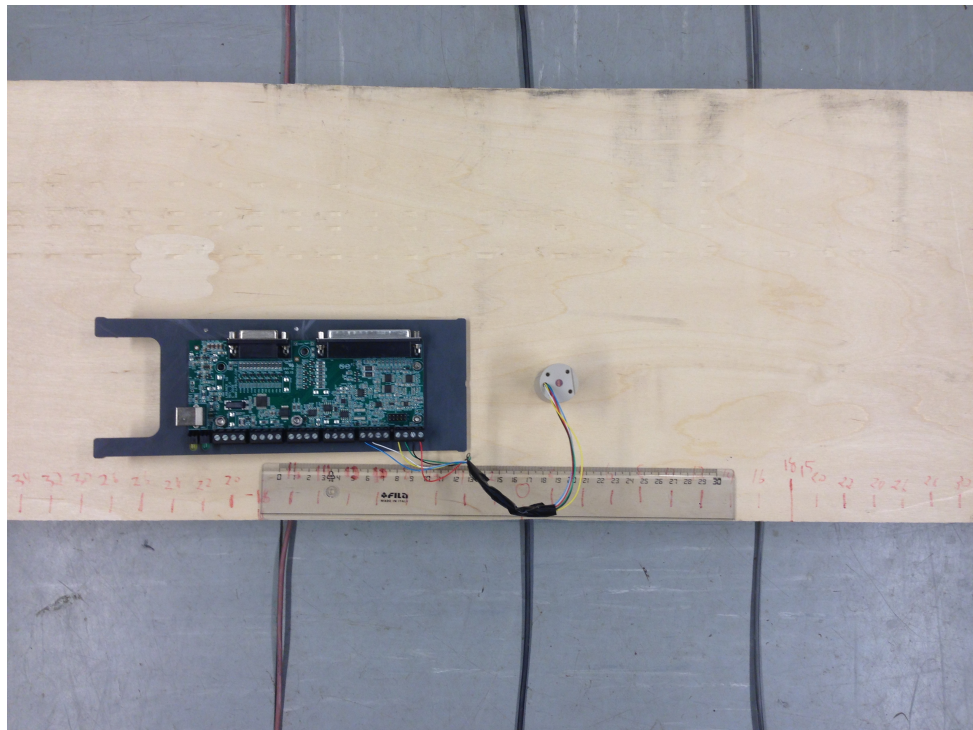


Figure 5.3: Three conductors in a three-phase system along with a Labjack DAQ and a FLC3-70 magnetometer. The cables are spaced 18cm apart and the table is 8cm over ground.

5.4 Nidaros cable

In Nidaros close by Trondheim Spektrum six single core TXSE are buried in the same trench. The map including marking of the location of cables is shown in figure 5.4

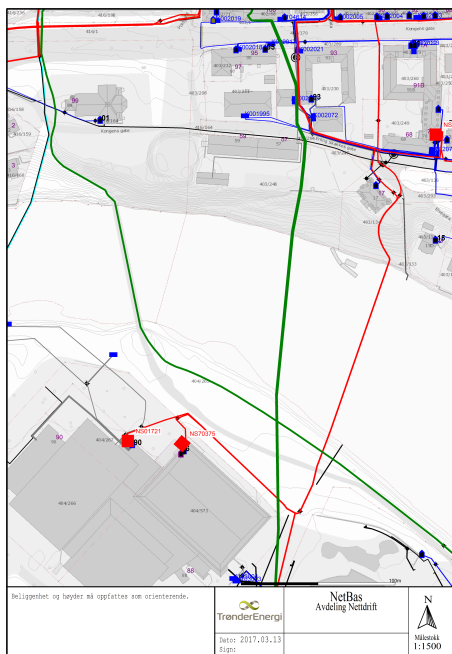


Figure 5.4: Map of cables at Nidaros. The building in the lower left corner is Trondheim Spektrum. Measurements were carried out on the six single core cables marked by a green line in the centre.

5.4.1 Set up

The device was moved from 6 meters to the side where the cable was supposed to be to 6 meters to the other side. At every 20 cm interval the magnetic field was measured. After this, the magnetic field was measured on what is believed is directly above the cable and gradually outward until no field could be detected.

5.5 Munkholmen cable

The cable to Munkholmen is a Tere 1kv twisted submarine cable by Nexans. The test was carried out on its land section at Korsivka where it goes into the sea.

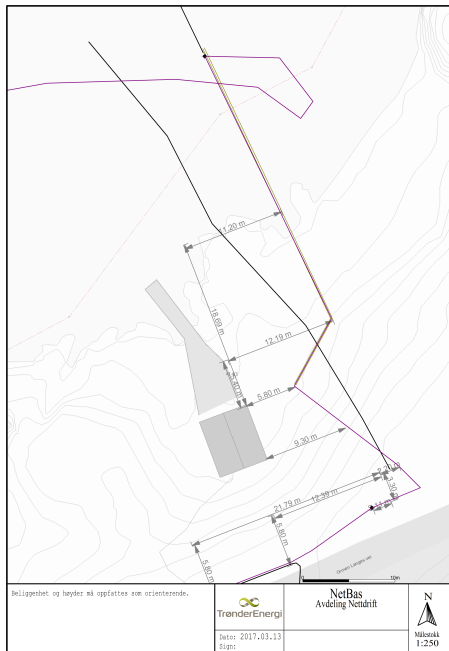


Figure 5.5: The right cable is the Tere 1kv cable at Korsvika going to Munkholmen. The left cable is out of operation



Figure 5.6: The Munkholm cable in Korsvika, marked by the lower right circle

5.5.1 Set up

The Magnetic field is measured when touching the cable and a small distance way from it.

5.6 Calibration

The calibration routines for compensating for both misaligned sensor axes and ferromagnetic distortions were carried out on REMUS 100 AUV. It's assumed that the AUV was lying perfectly flat. That is, the AUV z-axis was aligned to the earth's.

5.6.1 Set up

A single magnetometer was attached to the AUV and the AUV itself was placed on a carriage with wheels. The carriage was rotated in tight circles while the magnetometer sampled the field at regular intervals. Figure shows the REMUS 100 AUV with the fully mounted magnetometer module. Unfortunately, unforeseen circumstances prevented submarine cable survey with this full setup.



Figure 5.7: REMUS 100 AUV with the magnetometer module on front. The magnetometer are on each side of the front with a spacing of about 40cm.

Chapter 6

Results

6.1 Marine-Cybernetic Laboratory

6.1.1 Single Phase AC Cable

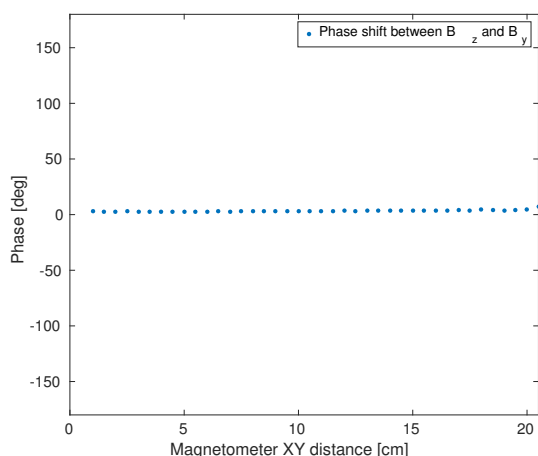


Figure 6.1: Relative phase between B_z and B_y with respect to the horizontal distance

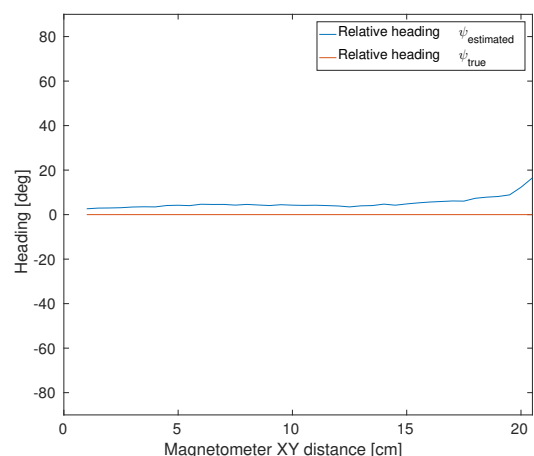


Figure 6.2: Relative heading between the AUV and the cable

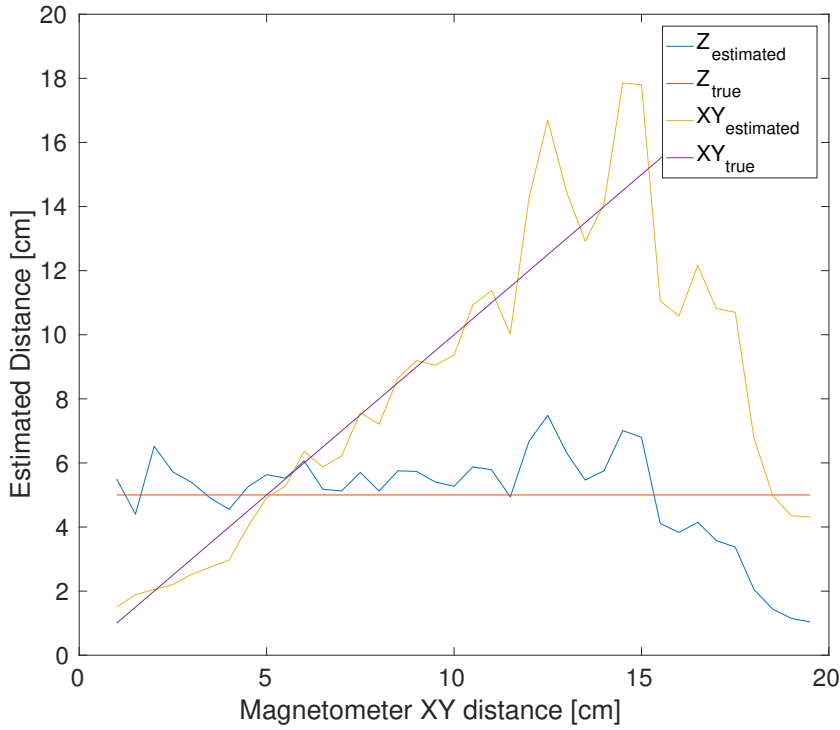


Figure 6.3: Estimated and true distance when the cable was moved away from the magnetometers

Figure 6.1, 6.3, and 6.2 shows the estimated and true parameters when the a single AC cable is moved away from the magnetometers at 1cm intervals. The true parameters must not be interpreted as literally true as they are a subject of measurements. As derived in section 3.2 B_y and B_z are in-phase if the cable is to the right the cable. This is the case in this experiment and Fig. 6.1 validates this with a phase shift very close to 0. The relative heading between the magnetometer and cable is shown in figure 6.2. The relative heading is very consistent at about 3° , which is very close to the true of 0° . The estimated position given in Fig. 6.3 is accurate until about 15 cm distance from the cable. From this point on the estimated position does not relate to the actual case.

6.1.2 Three-Phase Power System

Online

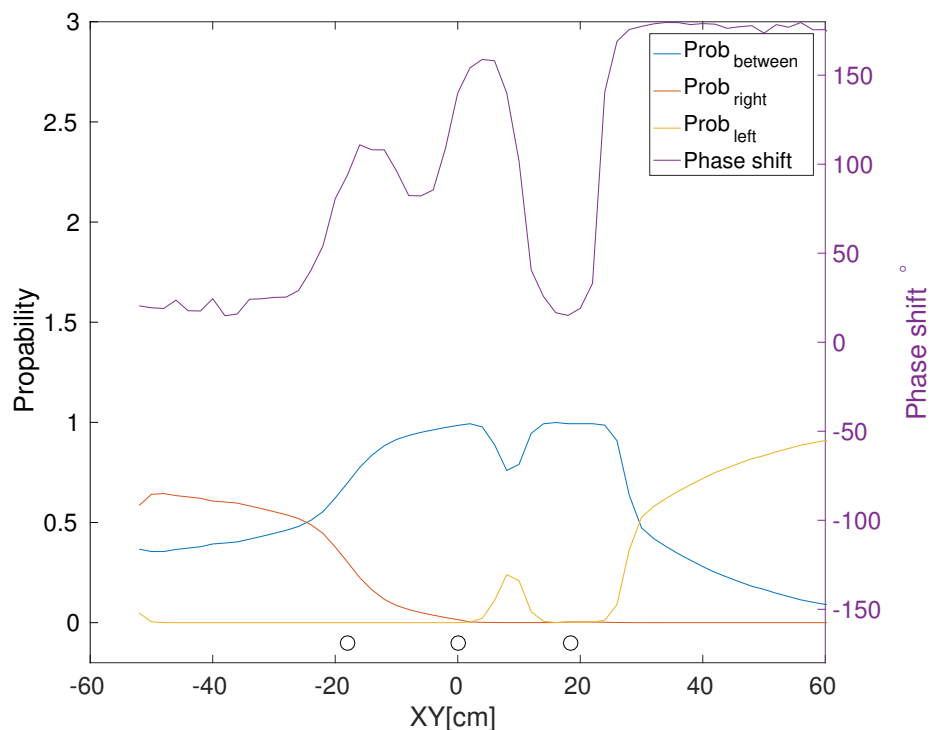


Figure 6.4: Estimation of the direction to the cables by the posterior probability function when crossing the cables. The purple graph shows the phase shift between B_{xy} and B_z and corresponds to the right y axis. The other lines are the probabilities for the direction to the cable. The weighting factor is tuned to $w = 0.001$. The cables' actual location are illustrated as circles in the bottom of the figure

Offline

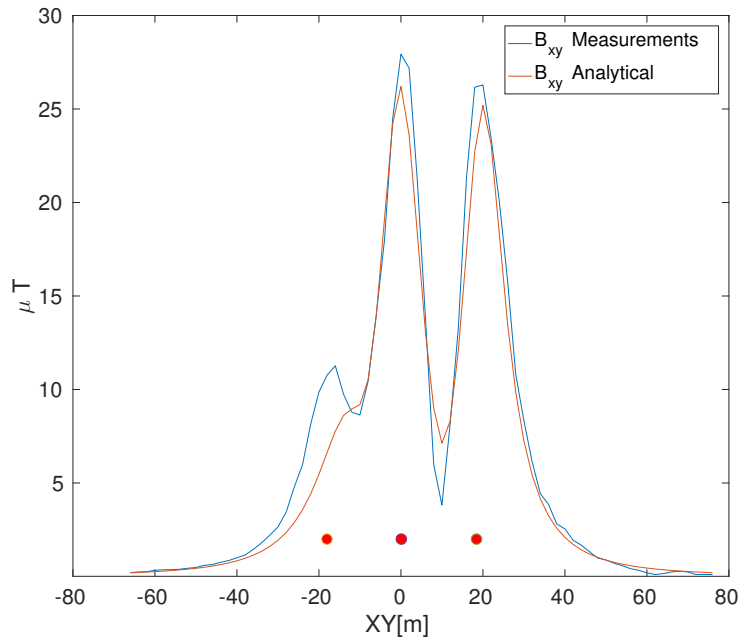


Figure 6.5: Curve fitting of Biot-Savart law to the measured B_{xy} when passing over the cables. The circles at the bottom illustrates the location of the cables

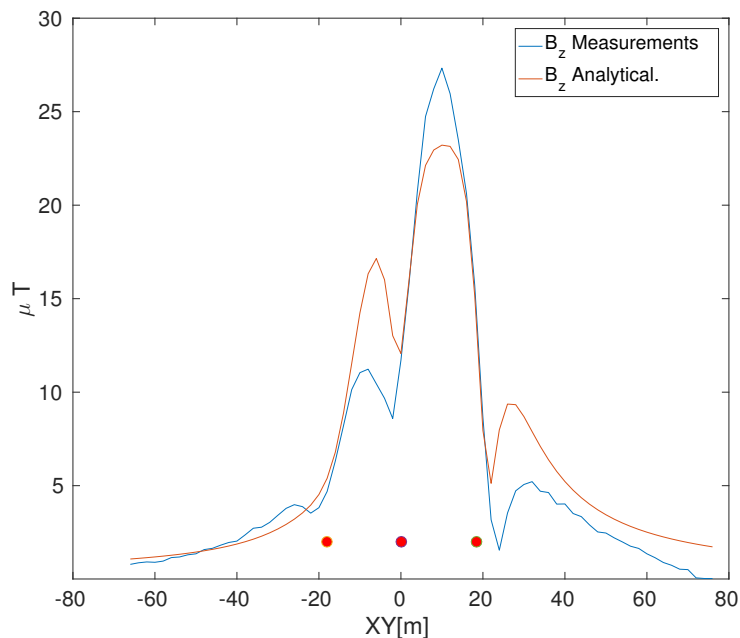


Figure 6.6: Curve fitting of Biot-Savart law to the measured B_z when passing over the cables. The circles at the bottom illustrates the location of the cables

Table 6.1: Estimated position of the three cables by the LSQ curve fit

Location	Actual Position [cm]	Curve Fitting (Biot-Savart Law) [cm]
C_{1xy}	-18	-14.8
C_{1z}	7.5	8.5
C_{2xy}	0	0.4
C_{2z}	8	7.9
C_{3xy}	18.5	20.0
C_{3z}	8	7.31
I_1	?	4[A]
I_2	?	7.3[A]
I_3	?	6.3[A]
Total Position Error	0[cm]	5.5[cm]

Figure 6.4, figure 6.6, along with table 6.1 shows the results for online and offline part of cable localisation from small-scale laboratory testing on three single core cables.

In figure 6.4 the phase shift start at zero and slowly builds up before crossing the first cable. Between the cables the phase shift varies, before it drops to almost zero before the last cable. When the outer right cable has been crossed the phase shift limits 180° . The probability of each situation follows the phase. P_{right} is largest until about $-23[cm]$, which is $5[cm]$ before the outer left cable. At this point it's surpassed by $P_{in-between}$. Lastly, when all the cables are crossed, P_{left} dominates. This occurs at about $30[cm]$.

These values are used as initial guesses for the positions in the LSQ Curve fitting algorithm. Comparisons of the curve fitted function and the measurements is seen in figure 6.5 and 6.6. Some discrepancy are apparent. For B_x the extremes are a bit understated and for B_z the outer peaks are overstated while the middle peak understated. The estimated location of the cables are given in table 6.1 where the total position error is $5.5[cm]$. The major part of this error is the first cable, which has an error of $3.2[cm]$. This is mostly caused by this conductor not transmitting the same amount of electricity and this wasn't perfectly compensated for.

6.2 Nidaros cable

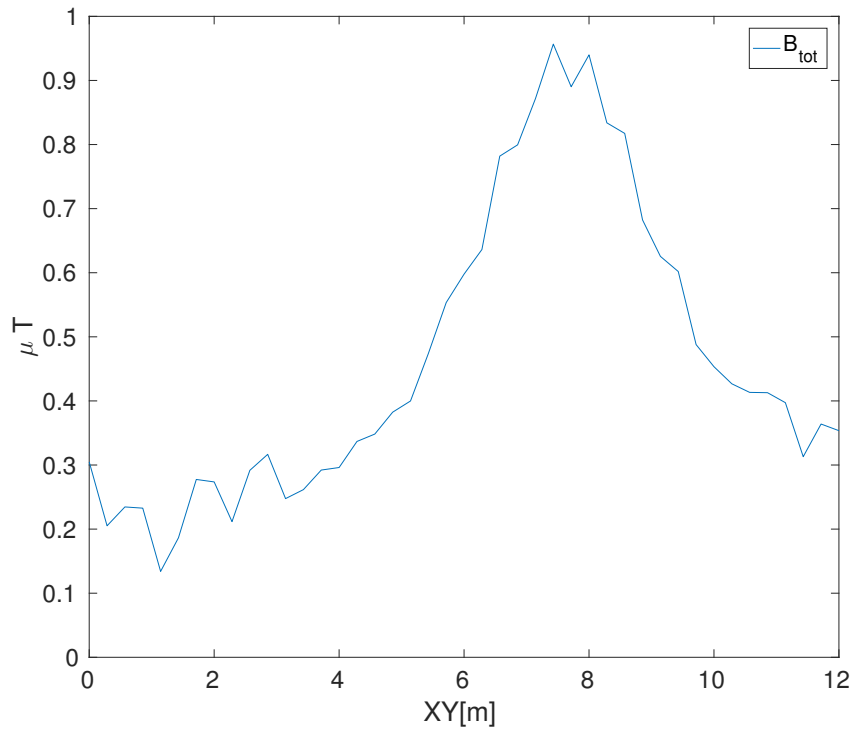


Figure 6.7: Magnetic flux density when crossing the trench containing the cables at Nidaros. The cluster are very likely located at about 8 meters from the start position

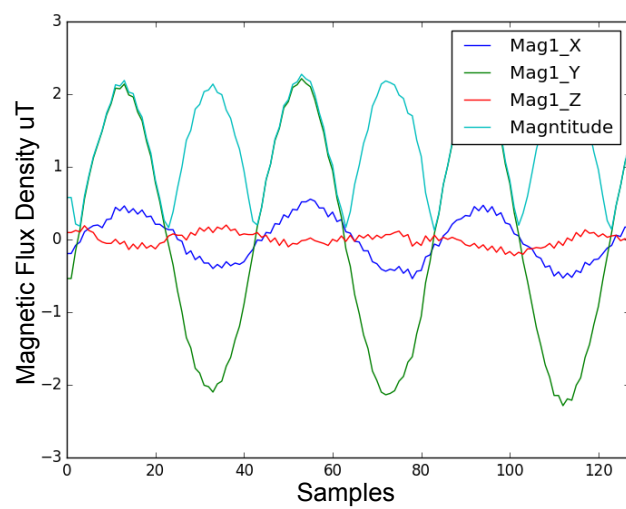


Figure 6.8: Magnetic flux density B_{tot} directly above the cables at Nidaros.

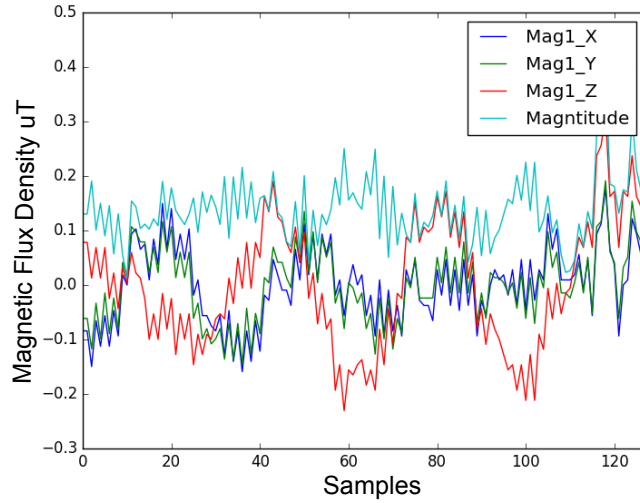


Figure 6.9: Magnetic flux density B_{tot} when 5m to the side of the cables at Nidaros.

Figure 6.7 shows the magnetic field when passing over the cables at Nidaros. It has a peak at about 8m from the start which corresponds to where the cables were marked on the map. Figure 6.8 shows samples of the magnetic field when allegedly directly above the cable¹ and figure 6.9 shows the magnetic field when 5 meters to the side. Both figures shows 128 samples which is roughly 0.06 seconds. This corresponds to about three period of the 50Hz magnetic field.

In Figure 6.8 its seen that B_z is low compared to the total field. This confirms measurements were made close to directly above the cables. Further, that the magnetometer was almost parallel to the cables, which can be seen from the relative strength between B_x and B_y . Actually, the relative heading is measured to be $\psi_{br} = 8^\circ$. When about 5 meter to the side of the cables Figure 6.9) the noise is almost as large as the amplitude of $B_{tot} = 0.2\mu T$. This much larger than the noise stated in the FLC3-70 data-sheet and is caused aliasing from the FLC3-70 magnetometer's 3[mV] (millivolt) ripple at a frequency of 17[kHz] [29]. This can be suppressed by an analogue lowpassfilter.

¹The peak does not correspond to fig 6.7 as the measurements where done at different days and the current in the cable varies.

6.3 Munkholmen cable

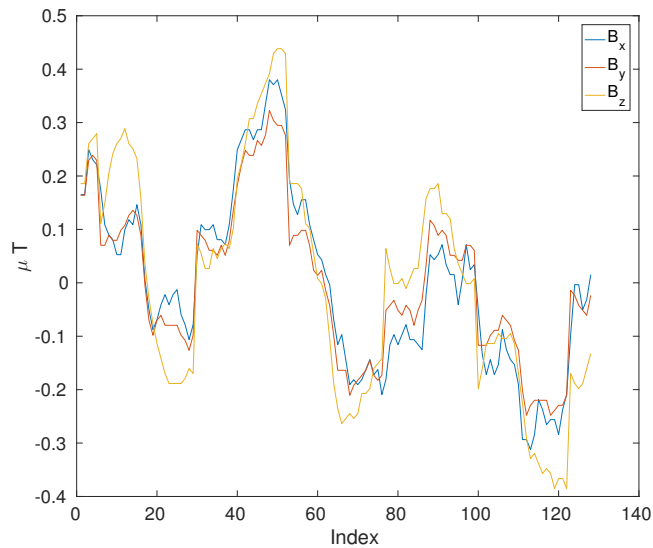


Figure 6.10: Magnetic flux density B_{tot} when physically touching the Tere 1kv cable with the magnetometer

As seen in figure 6.10 the magnetic flux density B is unpredictable and very small. The axes are all in the same phase. This is because the conductors are twisted. This makes the superposition of endless wires assumption void. The measurements with peak strength of $B_{tot} \approx 0.4\mu T$ are from measurements when physically touching the cable, any distance from it causes the 50Hz contribution to be just noise.

6.4 Calibration

6.4.1 Magnetometer Misalignment

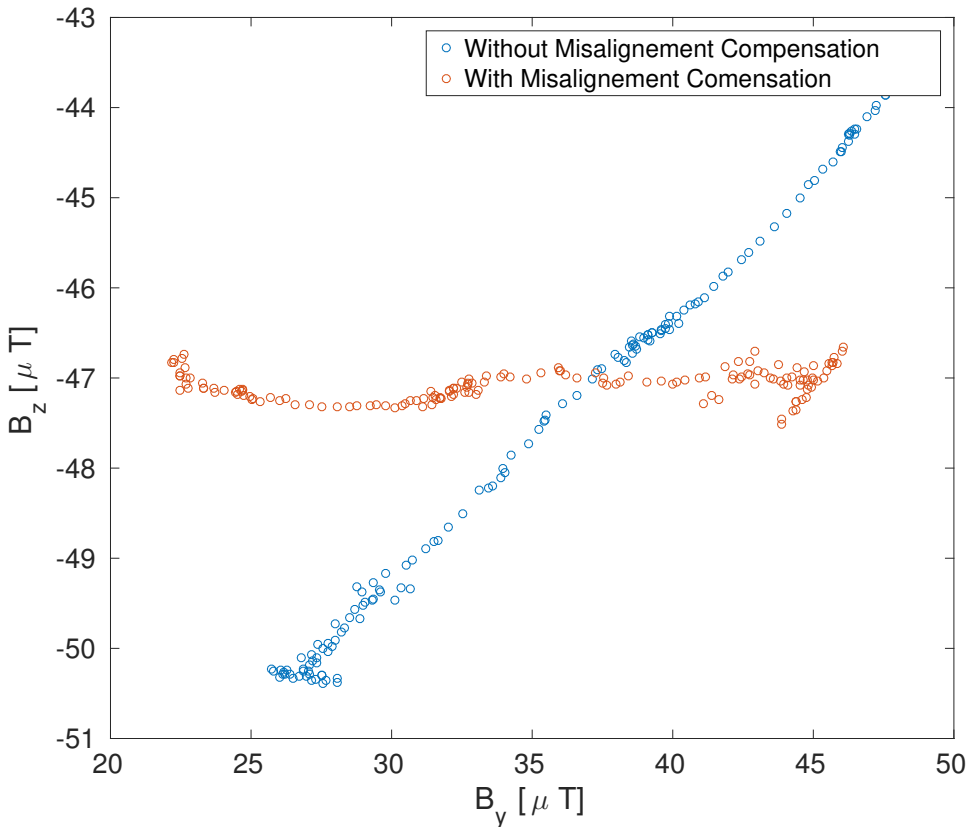


Figure 6.11: The results of compensating for magnetometer misalignment showing B_y field versus B_z field when the AUV is rotated in tight circles in yaw.

Fig. 6.11 shows the effect of compensating for the roll angle on the magnetometer. Initially the magnetometer's B_z did not align with that of the earth's vertical field and is therefore affected by its horizontal field. This can be seen by the blue scatter plot. By using the method presented in section 3.3.2 the roll angle was found and the the misalignment was compensated for. This can easily be seen in the orange scatter plot as B_z is almost independent of B_y and consequently, independent of the magnetometers heading. Note that B_y is not symmetric about zero as it's affected by an hard-iron distortion.

6.4.2 Ferromagnetic Distortion

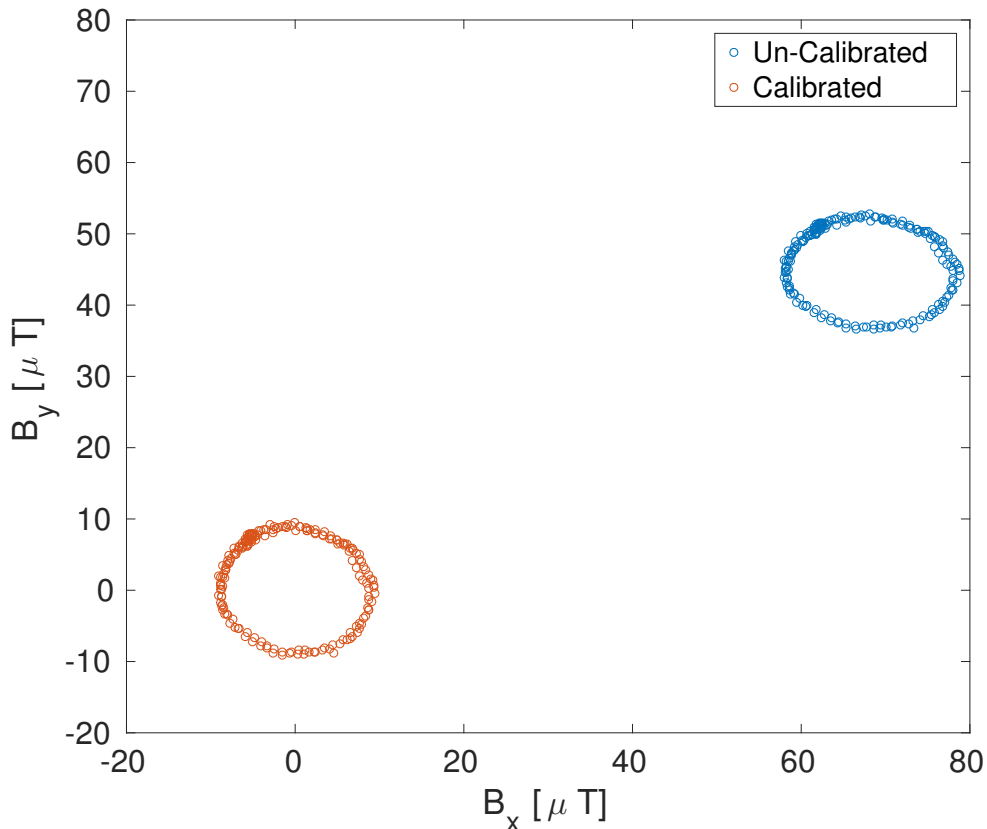


Figure 6.12: Ferromagnetic calibration results showing B_x field B_y when rotated in tight circles in yaw

The calibration for ferromagnetic distortion was carried out after the axes had been aligned and the results are presented in Fig. 6.12. As seen by the uncalibrated (blue) scatter plot the hard-iron distortion gave an initial origin of [70, 45]. It's is also slightly elliptical caused by soft-iron distortions. The principal axes are $r_x = 10.31, r_y = 7.87$. The orange scatter plot is after the calibration for ferromagnetic distortion. Its origin is in [0.12, 0.21] and the principal axes are $r_x = 9.3, r_y = 9.45$. Some of the soft-iron and hard-iron distortion is caused by the trolley on which the AUV lies. Nevertheless, the calibration routine is able to compensate for this as well.

Chapter 7

Discussion

In this chapter, the methods presented are discussed with respect to their applicability for submarine power cable survey with an AUV. The results from FEA and experiments are used as a basis for validating the methods.

At the time of carrying out this thesis a test survey was planned on cables at Nyhamna. This has highly influenced the focus of this thesis, and especially the finite element analysis. The methods can, however, be extended to the general case.

7.1 Magnetic fields

For a single cable the modelling of the magnetic field isn't crucial. This follows from only the relative strengths between B_z, B_x and B_y are used. And, as shown in figure 4.6, this is equal for all mathematical models. This is as expected as the effect of water, shield. etc. will effect all axes equally. Further, the introduced phased lag does not matter as there is no other sources the field it can have a phase shift to. This is the reason no derivations were made for the induced currents in a single cable solely because of self inductance. The only reason of having a more accurate description would be to estimate the required magnetometer sensitivity, and this far more accurate with FEA.

For a three-phase power system the field is much more complex. The field from each source are not in the same direction, neither are they peaking at the same time. Therefore each field had to be decomposed into two principal directions [34]. When combining these compo-

nents with Pythagoras theorem the resulting field is a purely mathematical expression. This follows from $B_{z_{tot}}$ and $B_{xy_{tot}}$ rarely occurs at the same time.

The effect of water was added by assuming that each cable was surrounded by a 320 cylinder of seawater and the current over this cross-section had to be zero. The field from three cables was achieved by superposition of the three cases. This mathematical model fits perfectly with the FEA as seen in figure 4.8. This also confirms that soil could be accurately be approximated as seawater, at least for one meter burial and soil conductivity of $\sigma = 1.5S/M$. Interestingly, the seawater had small effect on the decay of each field, but had a noticeable effect introduced by the phase lag. The phase lag depends on the distance the magnetic field had travelled in the sea. Therefore, at a given point, some fields have travelled farther and have greater phase lag than others. This caused the phase shifts between the magnetic fields on that point to be some other value than 120° . The effect of this was a greater peak if the fields at the point of measurement were more in-phase and a lower peak if the phase shift became closer to 180° . Therefore it makes sense that seawater had near-to-no effect on a single cable, but a rather great one on the three-phase power system. Technically, it can be said that the waters resistance is low, while its reactance is high.

With respect to finite element analysis the mathematical model of sheath-armour was very accurately described as seen in figure 4.9. Some simplifications were made; e.g. the inductance of the sea was ignored and sheath and armour were one non-magnetic unit. The simulations confirmed that ignoring the sea inductance didn't cause great errors. Actually, introducing seawater did not increase the overall error as seen in figure 4.10. Nevertheless, from [5] the medium of the three-phase power system can usually be neglected regarding inductance's when they are at least space 10[m] apart. This almost the case here, and for closer spaced cables ignoring this might not be valid.

When in air the max error between the FEA result and the mathematical model of the sheath-armour was only 7%. This is very low with regard to the field being about 60 times lower than without sheath and armour. On the other hand, the FEA model was intentionally designed to fit the assumptions in the derivation. To further validate the model more advanced finite element analysis should be made. Such as having an armour of wires twisted around the cable. Actually, twisting the armour wires will reduce the induced current in it [13]. As this current tends to negate the one in the conductor this will give an overall increase of the mag-

netic field. A more advanced FEA-model including this effect wasn't made as results showed that including the sheath-armour and effect of seawater only had marginally better results regarding cable localisation.

Including both the effect of seawater and sheath-armour the total field has a very similar curve. A comparison can be seen in figure 4.9. Except a tiny clockwise tilt the only discrepancy between FEA and the mathematical model is that the later is about 3% lower. Its' concluded that the derived model is very accurate compared to finite element analysis of a similar case.

7.2 Localisation of Single Phase AC Cables

The method for locating a single cable was tested on both simulations of a magnetic field and on a low-voltage conductor. This method has already been simulated with promising results in [36], and they are further confirmed here. It's also confirmed that increasing the magnetometer spacing helps suppress noise. This is clearly seen in Figure 4.15 and 4.16. REMUS 100 AUV is limited to a 40[cm] magnetometer spacing while Orion by optimal ranging recommends 1.5[m]. The simulations confirms that the accurate horizontal distance of locating the cables doubles from 5[m] to 10[m] when the spacing is increased.

A new method, proposed in this thesis, is to use the phase shift between B_z and B_y to determine the direction to the cable. From simulations, (Figure 4.17) this is possible for up to 30[m], six farther away than when localisation is accurate. It should be mentioned that SmartTrack claims a 30[m] distance for locating cables at currents as low as 150 milliampere[12]. This corresponds to about 1nT for an unshielded cable. This is not possible with the noise levels on FLC3-70 magnetometer. However, by using the phase shift SmartTrack could decide the direction to the cable at an even farther distance. Using this direction allows for the AUV to easily move within the range of accurate cable localisation.

FEA assumes perfect alignment of the sensors, full isolation of the cable's magnetic field and no ferromagnetic distortions. However, the experiments confirmed that using the phase shift allowed for finding the direction to the cable as a much greater distance. Also the relative heading was accurate for much longer. These results are presented in Figure 6.1 to 6.3. Finding the direction to the cable by the phase shift between B_z and B_y has a greater range

because the noise must be as large as the magnetic field peak to change the phase. On the other hand, just slight disturbances will disturb triangulation method.

7.3 Localisation of Three-Phase Power Systems

Two methods were formulated to track and locate the three cables. First, the triangulation method for one cable was used. This method should, ideally, locate the closest cable. The second uses an online part to track over the cables and then pinpoints their location post-survey by LSQ-curve fitting.

7.3.1 Single phase AC cable approximation

Figure 4.20 and figure 4.21 shows the localisation of three cables by triangulation method. With and without noise. From the latter case it's apparent that for 9m cable spacing and 4m hover height the method is unable to locate any of the cables. This is the method used by SmartTrack and apparently, 9[m] is, for the FLC3-70 magnetometers, a too close cable spacing for accurate localisation. To plan surveys it's beneficial to know a more specific definition of too close. However, it's difficult to derive an exact mathematical expression for when the one cable approximation will be valid. Generally, it's dependent on the cable's spacing compared to the hover height; i.e. if the AUV is flying very low, or the cables are spaced far apart the one cable approximation has a greater chance to be valid. Unfortunately, it's also dependent on the noise, and the magnetic field amplitude. All parameters were therefore set constant, except the cables' spacing which were gradually increased. Simulations with the triangulation method were then rerun until satisfactory results were achieved. Satisfactory was defined when the results were accurate for the same distance as for a single phase AC cable ($\pm 5[m]$). This occurred when the cable spacing was 30[m] and results from this case is presented in Appendix B. As a rule of thumb it's therefore stated that the single AC cable approximation is valid when distances between the cables are at-least 8 times the vertical distance to the AUV. This is of course a rough estimation and will change with respect to the magnetometers, cable layout, and the current in the conductors. Lastly, if the AUV is closer than 5m, the approximation is valid for a smaller cable spacing.

7.3.2 LSQ-Curve Fitting method

For a single AC cable the location of the cable is pinpointed directly and can be used for tracking. For a three-phase power system it's a bit more complex. This method is split into two. An online part used for tracking and an offline part used to pinpoint the location of the cables. The reason is that curve fitting is only possible after all cables have been passed and at this point the position couldn't be used for tracking anyway. Also, having a curve fitting algorithm on a on-board mini-computer is computationally demanding and will increase the time step between each series of samples.

Figure 4.22 and figure 6.4 shows that the results for the online tracking function from simulations and experiments, respectively. The posterior probability function accurately estimates the direction to the cable, or whether the AUV is between the outer cables. The weakness of the methods lies when between cables. To use a posterior probability function instead of using the phase shift directly was introduced to counter this problem. However, as this function has a forgetting factor that needs tuning the consistency of the method is questionable. Especially since the cables' spacing are all but consistent. Algorithms can be used that requires passing over three peaks before returning, but this has not been implemented, and it cannot be assured that not too many, or too few peaks are found. Nonetheless, the method is consistently accurate when outside all cables. By making the build up of probability very low and accepting a great overshoot of the outer cables this method is valid for zigzag guidance over three cables. Yet, no guarantee can be made that it will never give erroneous direction when in between. It should therefore not be the sole tracking parameter, but be combined with other sensors. For example: combined with a side-scan-sonar(SSS) the magnetometer can determine whether the cables are left or right and then the SSS can take over in between cables and ensure that all cables have been passed before returning. The SSS will naturally not work if the cables are completely buried. Another example is to use the pre-acquired location of the cables from Statnett SF and set up a zigzag route from this. The online code can then either be neglected, or used in conjunction with the predefined route.

For the simulated magnetic field, the offline LSQ-curve fit part is carried out for both Biot-Savart law in vacuum and the complete mathematical model including seawater and sheath-armour. The results in table 4.2 shows that the cable localisation is accurate for both, and only marginally more so when adding the extra effects. And this is when the FEA was made

with regard to the assumptions in the mathematical model; e.g. non-magnetic armour and seawater conductivity $\sigma_w = 5S/M$. For a real case the difference in accuracy should be even less. What really improved results is to introduce the conductor current as a parameter being tuned by the LSQ-curve fit algorithm. Effectively, this compensates for unknown currents and unmodelled effects in the cables' layout. As curve fitting uses many data points it's naturally far more robust against noise than triangulation. This was confirmed by having given accurate localisation of the cable with ten times the noise given for the triangulation method. The low-voltage three-phase power system was only curve fitted with respect to Biot-Savart law. This follows from the conductor being neither shielded, nor submerged in water. Still, the cable was accurately located (table 6.1, which confirms the results from the simulations and it can be concluded that the derived method is accurate in locating all cables in a three-phase power system.

The LSQ-curve fit is carried post-survey. This removes the need for fast processing. Thus, it might not be necessary to use the derived mathematical model at all. Instead a finite element model can be created of the cables' layouts. Now, by some optimisation algorithm (for example: particle swarm optimisation) the cables' locations can be tuned until the simulated magnetic field corresponds to the measured. The cables locations will then be more accurate than for any mathematical model. Further, this allows for far more complicated cable layouts, such as, twisted wires, magnetic shields and non-identical cables.

7.4 Triplex cables

Initially, it was believed that survey could be carried out on the Tere 1kv triplex cable between Korsivka and Munkholmen. Finite element analysis of an imaginary triplex¹ cable is shown in appendix C. Comparing the peak of the magnetic field over the triplex cable with the three single core cables (figure C.2 and figure 4.10) the peak magnetic is about the same. Measurements on the Tere 1kV cable, as shown in Figure 6.10, disproves this analysis as the magnetic field is not at all what expected. Firstly, the field is very small, more importantly, all the axes are in-phase. The latter does not correspond to superposition of three endless wires. This is caused by the conductors in the cable are twisted around each-other. This makes the super-

¹One cable with three conductors

position of three endless wires void and the magnetic field tiny. The effect of this is that the field is very difficult to detect, and if it is detected it can't be located as the underlying assumption of endless wires is void. As all submarine triplex cables in Norway are twisted[21] magnetic-based surveys on these is very difficult, if not impossible, and other methods are recommended.

7.5 Six single core cables

Measurements on the six single core cables buried at Nidaros showed that these can be detected by the device. Also the location of their burial can be determined by the peak of the magnetic flux density. The derived method for cable localisation was not implemented as this was initial testing of the device, and it was believed that further surveys on a submarine three-phase power system would be carried out. Nevertheless, it showed that the FLC3-70 magnetometer has far higher noise than expected from the data-sheet. This can be seen in figure 6.9. This is caused by a ripple of the magnetometer at about $3mV$ at a $17kHz$ frequency [29]. Aliasing from this ripple distorts the signal. To suppress this ripple, an analogue low-pass filter should be included in the device.

7.6 Calibration and misalignment compensation

As seen in figure 6.11, the derived routine compensates for the misaligned roll angle of the magnetometer compared to the AUV. The established routine assumed that the magnetometer had no relative heading, nor relative pitch to the AUV. The assumption regarding heading is valid as the magnetometer casing is mounted by a straight steel bar perpendicular to the AUV body. However, the steel bar is threaded and connected to the AUV by nuts. This gives a possibility for the magnetometer and AUV to have a misaligned pitch angle. Compensating for this as well will greatly increase the complexity of the routine.

The ferromagnetic distortions were successfully calibrated for as can be seen in figure 6.12. As mentioned before, the hard-iron distortion is of minor importance regarding AC cable localisation. This comes from the fact that it's static and will therefore be filtered out by the Fourier transform. The soft-iron contribution, however, will skew the cable generated field

as well. This can will cause errors, especially for the triangulation method. As seen in figure 6.12 the calibrated plot is almost perfectly circular confirming that the soft-iron distortions have been calibrated for. This being said, the uncalibrated plot wasn't very elliptical in the first place.

The calibration routine and misalignment compensation presented in the results are from an initial test of the methods before the magnetometer casings had arrived. Therefore the routine was carried out while the AUV was on land and positioned on a trolley with wheels. The uncalibrated plots should therefore not be given much attention, however, the successfully calibration, even with extra effect of the trolley, confirms that the simple calibration routine presented is satisfactory for REMUS 100 AUV.

7.7 Non-Transmitting Cables

Non-transmitting cables were initially not a concern for this thesis. However, Statnett SF inquired whether it was possible to locate a ferromagnetic pipe with the same equipment as used for locating power cables. A proposed method is given in appendix D. The method presented is more or less unaltered to the method given by Innovatum in [12]. With other words, detecting the horizontal-location of ferromagnetic non-transmitting pipes is possible. Its buried depth is more complex as much must be known of the cable's layout and its intrinsic magnetic field. However, Statnett SF is mostly interested in where it's buried so trenches for new cables are dug m elsewhere.

Little configuring is needed to go from transmitting cable survey to non-transmitting cable survey. Firstly some code must be implemented to extract the static magnetic field, but this is rather trivial and easily obtained by the zero frequency component of the Fourier transform. The next step is to place the magnetometers on the vertical BODY-axis instead of the horizontal. This is not ideal for transmitting cable localisation as it will cause a singularity when directly above the cable. Naturally, by investing in four magnetometers both methods can be operational simultaneously. The method presented in [12] finds the peak of the vertical component of the gradiometer. Theoretically, it should be possible to use the absolute value instead as this reduces the need of perfectly aligned magnetometers in the gradiometer pair. However, this has not been tested.

Chapter 8

Concluding Remarks

8.1 Conclusion

A mathematical model for the magnetic field around a three-phase power system was derived. The model accounts for the effect of both shielding and seawater, and it was verified by comparison with finite element analysis. Further, the model was used to design and implement a method for locating and tracking cables in a three-phase power system. The localisation is carried out post-survey, while the tracking is performed online. Both simulations and experiments confirmed that the method is accurate for locating the cables. Adding the effect of seawater and shielding gave only marginal improvements in terms of estimation accuracy. For cable tracking, the method is accurate when on either side of the three-phase power system. When in-between the cables, there is a risk of a wrong direction being given. Nevertheless, this did not happen either for simulations or experiments.

The simulations used was a representation of the three-phase power system at Nyhamna, Molde. For this simulation, it was confirmed that single cable approximation, as used by SmartTrack, is not valid at 9 meters cable spacing. Further simulations gave the necessary spacing to be 30 meters. It's concluded that one cable approximation is valid when the cables' spacing is at least 8 times the AUV's hover height. These results are, however, dependent on cable specific parameters, and magnetometer accuracy.

A method was established to decide the direction the cable by the phase shift between magnetic field components. For a single AC cable both simulations and experiments confirmed

that locating the direction to the cable this way between allowed for tracking to the cable from much farther distances than when using the triangulation method alone.

A device for carrying out magnetic-based cable survey with REMUS 100 AUV was developed. Both single cable localisation and tracking of a three-phase power system were implemented. All experiments were carried out with this device and the results from the tests concurred with the results from the simulations. Lastly, calibration routines have implemented and tested on REMUS 100 AUV. Results from these proved them successful.

8.2 Further Work

Most importantly, a submarine cable survey should be carried with REMUS 100 AUV and the device created as a part of this thesis. All code and equipment has been implemented and an actual survey is all that remains. Preferably the survey should be carried out on a three-phase power system to validate the new method derived.

Further, to improve accuracy, an analogue lowpass filter should be included in the device. This will remove the 17kHz voltage ripple that effect the magnetometer readings by aliasing.

A more advanced calibration routine should also be implemented. This routine should focus on an optimised calibration of the soft iron distortion. This can for example be performed by an ellipsoid fit [8]. Further, the misalignment compensation should take into account the misalignment in both pitch and roll.

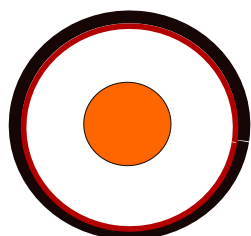
Lastly, and optimisation algorithm can be implemented to work in conjunction with a finite element analysis program. This could possibly give an even more accurate location of the cables.

Appendices

Appendix A

Validation of FEM-modelling

To confirm correct modelling technique of the finite element analysis a cable is designed which designed equal to what is used in [28]. In this article the FEA results corresponded to measurements at a similar real life case. parameters are given in the table below



Element	Description	Value
Conductor	Solid Copper wire.	50mm
Insulator	Acrylic plastic	28mm
Metallic Shield	Steel	2mm
Insulator outer	Acrylic Plastic	5mm
Seawater	Conductivity	$\sigma = 4S/m$
Steel	Conductivity	$\sigma = 5 * 10^6 S/m$
Steel	Permeability	$\mu_r = 300$
Acrylic Plastic	Conductivity	$\sigma = 10^{-12} S/M$

Figure A.1: Single Phase AC cable as used in for the FEM-model in [28]. Items not in the table are assumed to have $\mu_r = \epsilon_r = 1$.

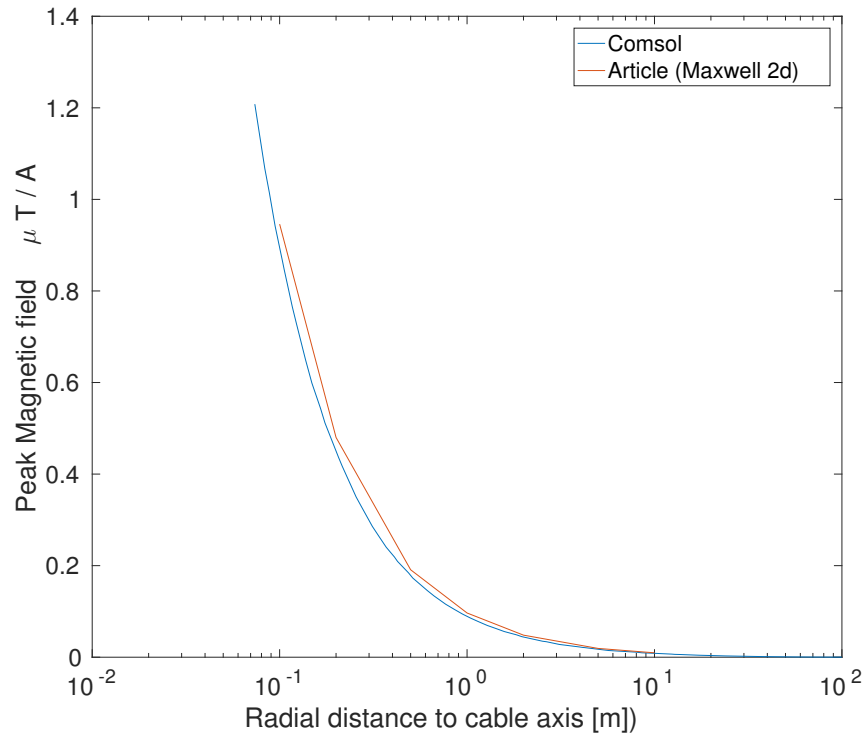


Figure A.2: Comparison of the magnetic field for two identical models made in Comsol and Maxwell2D

Figure A.2 Comsol Analysis for a shielded cable is compared to the solution in [28]. The concurrence between the is apparent. The small discrepancy might be caused by different conductor material, mesh size and numerical round off between Comsol and Maxwell 2D.

Appendix B

Single Cable Approximation

The finite element of model of Nyhamna had it's cable spacing gradually increased until the one cable approximation was valid for up to $\pm 5[m]$ distance to the cable. All else is identical, including the noise and conductors currents. Sufficient accuracy occurred with a cable spacing of 30m and the localisation can be seen in figure B.1 and figure B.2. A small spike occurs when directly above the cable as is clear in figure B.2 with $XY = -30$. This happens because B_z of the closest cable is zero and the magnetic peak in z is therefore decided by the peak magnetic field caused by the two other cables.

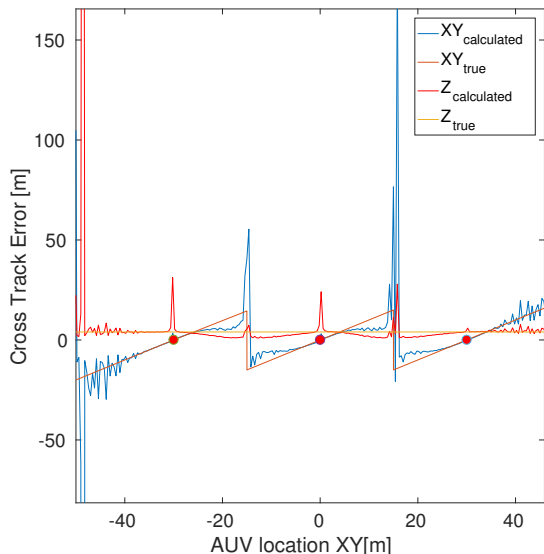


Figure B.1: Cable localisation when crossing over cables with 30 meter spacing

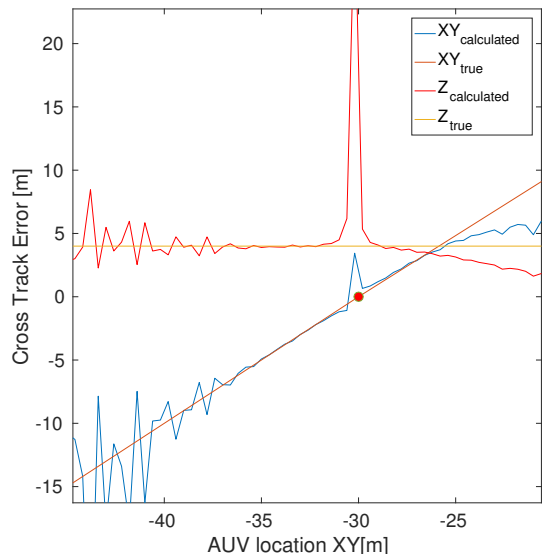
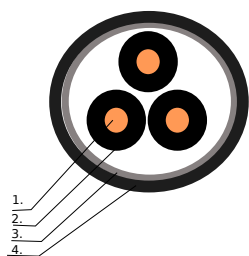


Figure B.2: Outcrop of the leftmost cable

Appendix C

Triplex Cable

Finite element analysis was carried out for a fictive triplex cable. In this model all the conductors are straight.



Element	Description	Thickness
1. Conductor	Solid Copper wire.	18.3mm
2. Insulator	Acrylic plastic	5.5mm
3 Armour	Steel wire	4.2mm
4. Insulator outer	Acrylic Plastic	4mm

Figure C.1: Single Phase AC cable

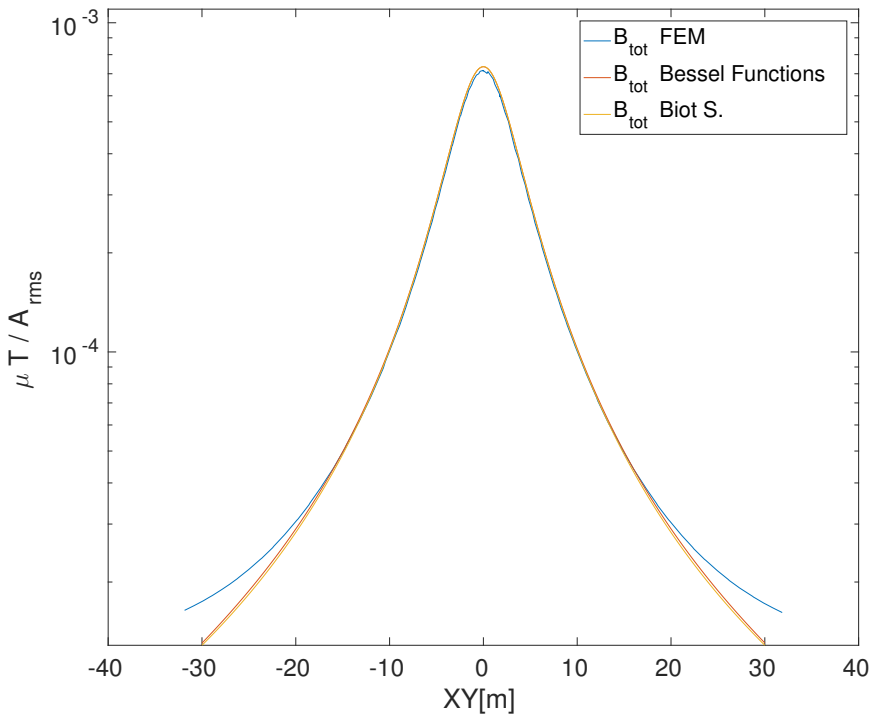


Figure C.2: The two analytic models are almost identical while FEM diverges away at about 20m. The two mathematical models only differ in the effect of saltwater. Here they are identical because the conductors are almost at the same place which makes the field move almost equal distances in saltwater giving near to no extra phase shift.

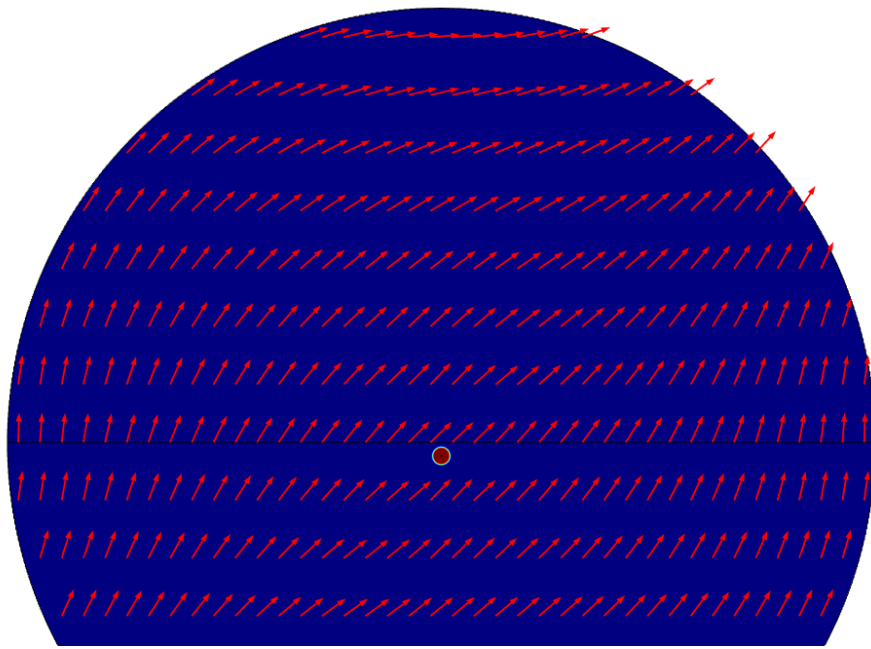


Figure C.3: Direction of the field from non-twisted triplex cable

The resulting magnetic field over a triplex cables is seen in C.2. The maximum peak is similar to three single core cables and can be tracked and located. However, the triplex submarine cables used in Norway are twisted [21]. This means that the three conductors are twisted around each other. The effect of this is that total the magnetic field tiny and can not be expressed by a superposition of endless wires. This is confirmed by measurements on the Munkholmen cable (Figure 6.10). Therefore magnetic based cable survey are deemed impractical, if not impossible, on triplex cables in Norway.

Appendix D

Ferromagnetic pipe detection

This section is about the location of pipes or cables not transmitting electricity, but containing some ferromagnetic material. Some examples are oil-pipes, gas-pipes and outdated power cables with magnetic armour wires. The following method is based on the theory of operation for the SmartrTrack system by Inovatum [12].

A ferromagnetic pipe will produce a magnetic field from two different sources. Intrinsic magnetisation, and induced fields.

D.1 Intrinsic magnetisation

When the pipe section was molten the electrons aligned depended on the magnetic field at the present time and location. When the material was solidified ¹ this alignment remained and an intrinsic magnetic field was created. When looking along the pipe this field tends to point radially toward or away from the pipe centre [12].

D.2 Induced Magnetic field

Magnetic fields will be induced in ferromagnetic materials by the Earth's magnetic field. The strength of the induced field is dependent on the Earth's magnetic field at the location and

¹Specifically, when it passed through its Curie temperature [12].

the materials magnetic permeability μ . This field will be aligned with the earth's and thus vary in the direction depending on pipes latitude coordinate.

D.3 Localisation method

For localisation of the pipes it is beneficial to determine what is directly above the field. As mentioned the intrinsic field has mostly a radial field and above the pipe this is solely a vertical component. Further, Statnett SF is mostly interested in submarine located in Norway. At this latitude the earth's magnetic field is mostly vertical. The vertical component of the pipe is the sum of these.

In [12] the field was measured to 775nT 3 meter above a 12-inch steel pipe. This is large enough to be detected by good magnetometer, however the earth's magnetic field in Norway is about 100 times as strong. Thus, the main concern is therefore to detect the pipe's field when the earth's is so dominating. SmartTrack [12] does this by the use of a *gradiometer*.

Earth's magnetic field only varies notably in distances of about 100 of meters, while the field from the pipe will change from much smaller distances. By placing two magnetometers on the same vertical axis the field of one can be subtracted from the other. The difference represents the decline of the magnetic of the field between the two magnetometers and should be largest directly above the cable. This setup of magnetometers is called a gradiometer and is illustrated on an AUV in Fig. D.1.

By continuously guiding the AUV towards the biggest difference of the magnetometers vertical component the AUV will track along the pipe. As the earth's field is very much stronger than the cable's high accuracy is required of the alignment of the magnetometers. Misalignment can be compensated before survey by a calibration.

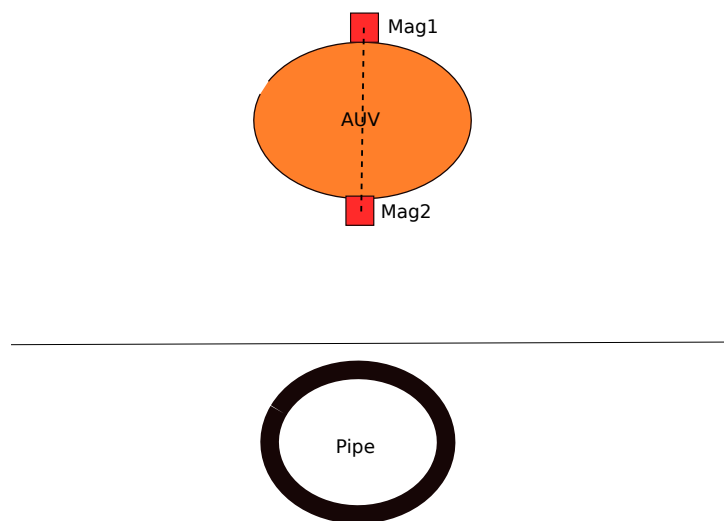


Figure D.1: A pipe, the AUV and two magnetometers in a gradiometer setup

Bibliography

- [1] R. R. Alabern Morera. Effects of the circulating sheath currents in the magnetic field generated by an underground power line. 2006.
- [2] A. Ballari. Person, communication.
- [3] A. Ballari. Person, communication.
- [4] G. Bianchi. Induced currents and losses in single-core submarine cables. IEEE Transactions on Power Apparatus And Systems, 95:59 – 68, 1976.
- [5] I. E. COMMISSION. Electric cables–calculation of the current rating part 1: current rating and calculation of losses1. iec, 1994.
- [6] Comsol. Submarine Cable 4 Inductive Effects, 2016. Rev. 1.1.
- [7] W. E.T. A History of the Theories of Aether and Electricity. Dover Publications, 1951.
- [8] Freescale Semiconductor. Calibrating an eCompass in the Presence of Hard- and Soft-Iron Interference, 2015.
- [9] W. Frei. Computational electromagnetics modeling, 2013.
- [10] H. E. Haber. Adding sines. <http://scipp.ucsc.edu/~haber/ph5B/addsine.pdf>, 2009. Accessed :2017-05-18.
- [11] P. Hassani Hespanha, Athans. Stability analysis of rmmac, 2011.
- [12] Inovatum. INNOVATUM PRODUCT REFERENCE MANUAL. 2012.
- [13] G. A. J.S Barret. Circulating current and hysteresis losses in screens sheaths and armour of electric power cables- mathematical models and comparison with iec standard 287. IEE Proc.-Sei. Meas. Technol., 144, 1997.

- [14] Kjetså. Underground electrical cable localisation by magnetometers on remus 100 auv. unpublished thesis, 2016.
- [15] J. Kjolleberg. The use of magnetometers on hugin to identify hydrothermal vents, 2014.
- [16] E. Kreyszig. Advanced Engineering Mathematics. Wiley, 2011.
- [17] P. P. L. Jiang. Operatin-state monitoring and energization-satus identification for underground power cables by magnetic field sensing. 2013.
- [18] T. D. Mateer. The Fast Fourier TransformA Mathematical Perspective. Wiley, 2008.
- [19] I. Matusmoto. Real-time vision-based tracking of submarine-cables for auv/rov. n, 9(4):1997–2002, 1995.
- [20] D. Meeker. Current induced in steel tipe. <http://www.femm.info/wiki/TubeExample>, 2001. Accessed:2017-05-19.
- [21] Nexans. Kabelboka,haandbok for e-verkskabler.
- [22] S. R. Norgren, Petter. Using autonomous underwater vehicles as sensor platforms for ice monitoring. pages 263 – 277, 2014.
- [23] N. P. on Technology Enhanced Learning. Inductance of three-phase lines with asymmetrical spacing. http://nptel.ac.in/courses/Webcourse-contents/IIT-KANPUR/power-system/chapter_1/1_7.html, 2015. Accessed : 2017-05-19.
- [24] Optimal Ranging. Orion Manual, 2014. Rev. 1.1.
- [25] E. M. Purcell and D. J.Morin. Electricity and magnetism. Cambridge, 2013.
- [26] F. W. Sears and M. W. Zemansky. University Physics: Third Edition (Complete Volume). Addison-Wesley Publishing Company, 1964.
- [27] F. Sims, D. Lainiotis, and D. Magill. Recursive algorithm for the calculation of the adaptive kalman filter weighting coefficients, April 1969.
- [28] S. Slater, Jones. The prediciton of electromagnetics fields generated by submarine power cables, 2010.
- [29] Stefan Mater Instruments. Magnetic Field Sensor FLC3-70 Operation Manual, 2010.

- [30] R. Stoll. The Analysis of Eddy currents. Oxford Press, 1964.
- [31] Teleopgraphy. Teleopgraphy. <https://www.telegeography.com/research-services/global-bandwidth-research-service/index.html>, 2013. Accessed:2017-06-09.
- [32] Thor.Fossen. Handbook of Marine craft hydrodynamics and motion control. McGraw Hill, 2012.
- [33] J. Vanderplas. Understanding the fft algorithm. <https://jakevdp.github.io/blog/2013/08/28/understanding-the-fft/>, 2013. Accessed:2016-09-20.
- [34] A. Vistnes. Lavfrekvente elektromagnetiske felt. 2006.
- [35] T. Worzyk. Submarine Power Cables - Design, Installation, Repair, Environmental aspect. Springer, Berlin Heidelberg, 2009.
- [36] N. Z. Xiang, Yu. Subsea cable tracking by autonomous underwater vehicle with magnetic sensing guidance. n, 9(4):22, 2016.
- [37] R. Zhang, Y. Duan, S. Or, and Y. Zhao. Smart Elasto-Magneto-Electric (EME) Sensors for Stress Monitoring of Steel Cables: Design Theory and Experimental Validation. Sensors, 14(8):13644–13660, 7 2014.